



HAL
open science

Aquaporin-4 Surface Trafficking Regulates Astrocytic Process Motility and Synaptic Activity in Health and Autoimmune Disease

Silvia Ciappelloni, Delphine Bouchet, Nadège Dubourdiou, Eric Boué-Grabot, Blanka Kellermayer, Constance Manso, Romain Marignier, Stéphane H.R. Oliet, Thomas Tourdias, Laurent Groc

► **To cite this version:**

Silvia Ciappelloni, Delphine Bouchet, Nadège Dubourdiou, Eric Boué-Grabot, Blanka Kellermayer, et al. Aquaporin-4 Surface Trafficking Regulates Astrocytic Process Motility and Synaptic Activity in Health and Autoimmune Disease. *Cell Reports*, 2019, 27 (13), pp.3860-3872.e4. 10.1016/j.celrep.2019.05.097 . hal-02346691

HAL Id: hal-02346691

<https://hal.science/hal-02346691>

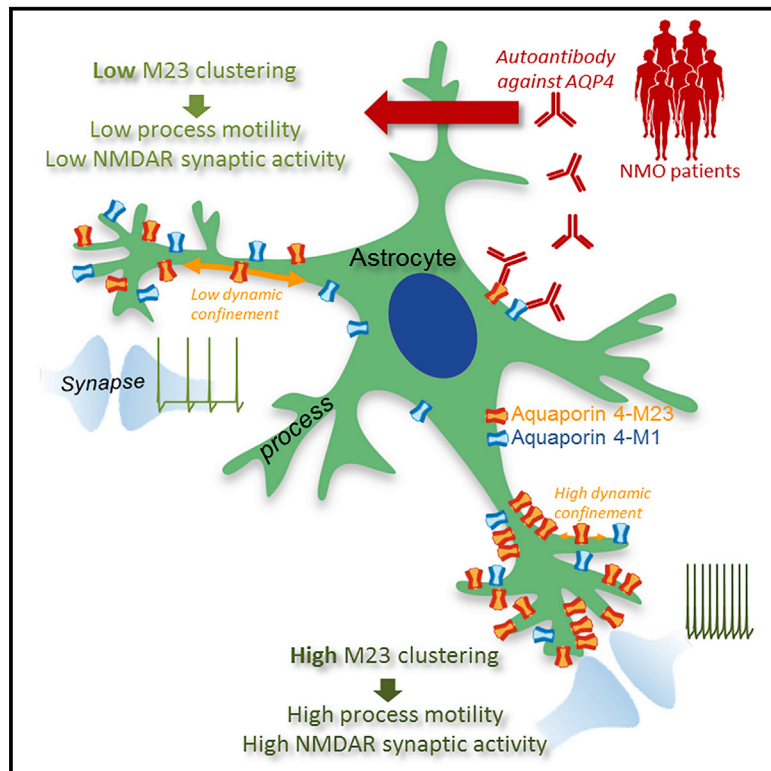
Submitted on 5 Nov 2019

HAL is a multi-disciplinary open access archive for the deposit and dissemination of scientific research documents, whether they are published or not. The documents may come from teaching and research institutions in France or abroad, or from public or private research centers.

L'archive ouverte pluridisciplinaire **HAL**, est destinée au dépôt et à la diffusion de documents scientifiques de niveau recherche, publiés ou non, émanant des établissements d'enseignement et de recherche français ou étrangers, des laboratoires publics ou privés.

Aquaporin-4 Surface Trafficking Regulates Astrocytic Process Motility and Synaptic Activity in Health and Autoimmune Disease

Graphical Abstract



Authors

Silvia Ciappelloni, Delphine Bouchet, Nadège Dubourdiu, ..., Stéphane H.R. Oliet, Thomas Tourdias, Laurent Groc

Correspondence

laurent.groc@u-bordeaux.fr

In Brief

Ciappelloni et al. use fluorescent imaging approaches to investigate how astrocytes control their highly ramified processes. The membrane dynamics and distribution of aquaporin-4 (AQP4) subtypes control the motility of astrocyte processes, influencing the physiological interplay between astrocyte and neurons. This regulation is targeted by autoantibodies from NMO patients.

Highlights

- AQP4 subtypes have different membrane trafficking and distribution in astrocytes
- AQP4-M23 membrane dynamics are regulated by neuronal activity
- AQP4-M23 membrane dynamics tune astrocyte process motility and synaptic transmission
- Autoantibodies from NMO patients disturb AQP4 surface dynamics and related functions



Aquaporin-4 Surface Trafficking Regulates Astrocytic Process Motility and Synaptic Activity in Health and Autoimmune Disease

Silvia Ciappelloni,^{1,2,3} Delphine Bouchet,^{1,2} Nadège Dubourdieu,^{2,3} Eric Boué-Grabot,^{2,4} Blanka Kellermayer,^{1,2} Constance Manso,^{1,2} Romain Marignier,⁵ Stéphane H.R. Oliet,^{2,3} Thomas Tourdias,^{2,3,6} and Laurent Groc^{1,2,6,7,*}

¹Interdisciplinary Institute for NeuroSciences, CNRS UMR 5297, 33077 Bordeaux, France

²Université de Bordeaux, 33077 Bordeaux, France

³INSERM U1215, Neurocentre Magendie, 33077 Bordeaux, France

⁴CNRS, Institut des Maladies Neurodégénératives, UMR 5293, 33000 Bordeaux, France

⁵INSERM U1028, CNRS UMR 5292, Center for Research in Neuroscience of Lyon, Lyon, France

⁶Senior author

⁷Lead Contact

*Correspondence: laurent.groc@u-bordeaux.fr

<https://doi.org/10.1016/j.celrep.2019.05.097>

SUMMARY

Astrocytes constantly adapt their ramified morphology in order to support brain cell assemblies. Such plasticity is partly mediated by ion and water fluxes, which rely on the water channel aquaporin-4 (AQP4). The mechanism by which this channel locally contributes to process dynamics has remained elusive. Using a combination of single-molecule and calcium imaging approaches, we here investigated in hippocampal astrocytes the dynamic distribution of the AQP4 isoforms M1 and M23. Surface AQP4-M1 formed small aggregates that contrast with the large AQP4-M23 clusters that are enriched near glutamatergic synapses. Strikingly, stabilizing surface AQP4-M23 tuned the motility of astrocyte processes and favors glutamate synapse activity. Furthermore, human autoantibodies directed against AQP4 from neuromyelitis optica (NMO) patients impaired AQP4-M23 dynamic distribution and, consequently, astrocyte process and synaptic activity. Collectively, it emerges that the membrane dynamics of AQP4 isoform regulate brain cell assemblies in health and autoimmune brain disease targeting AQP4.

INTRODUCTION

Astrocytes are essential cells of the CNS, ensuring key metabolic and signaling functions in brain cell assemblies. They have high morphological complexity with extended and ramified processes that are intimately associated with synapses both at the structural level through the coverage of spines and presynaptic terminals and at the functional level through the release of gliotransmitters (Halassa and Haydon, 2010; Panatier et al., 2006; Theodosis et al., 2008; Volterra and Meldolesi, 2005) and

the uptake of neurotransmitters. Astrocytes can, in addition, sense neuronal activity and rapidly restructure their processes near synaptic elements (Bernardinelli et al., 2014; Oliet et al., 2001; Perez-Alvarez et al., 2014). The movement of water through the plasma membrane constitutes one of the main hypothetical pathways by which astrocytes tune their volume and regulate the motility of their processes (Reichenbach et al., 2010). Indeed, astrocytes rapidly swell or shrink in response to a shift of osmolytes and water between the extracellular and intracellular compartments (Mongin and Kimelberg, 2005). In astrocytes, water movement is mediated mostly by the water channels aquaporin-4 (AQP4) (Kimelberg, 2004; Manley et al., 2000), which are located predominantly onto perivascular endfeet (Nagelhus and Ottersen, 2013) and, to a lesser extent, onto processes facing excitatory synapses (Amiry-Moghaddam and Ottersen, 2003). AQP4 exists in two main isoforms, M1 and M23, which exhibit similar water transport capacities but different aggregation properties and cellular distribution onto astrocytes (Crane et al., 2010; Smith et al., 2014). At the structural level, the two isoforms have similar extracellular domains but different intracellular ones (Crane et al., 2010; Smith et al., 2014). In addition, these two isoforms have different surface-trafficking characteristics in pure cultured astrocytes (Crane et al., 2008, 2010). Thus, the possibility that AQP4 isoforms differentially control astrocytic process motility, through distinct membrane organization, has emerged and gained support.

Using a combination of super-resolution, single-molecule, and calcium imaging approaches, we here demonstrated that the surface trafficking of AQP4 isoforms differentially modulates astrocytic process motility and excitatory neurotransmission. By imaging astrocytic motility and neuronal Ca^{2+} transient while artificially immobilizing AQP4 onto astrocytes, we demonstrated that among the two isoforms, the surface trafficking of AQP4-M23 mainly regulates astrocyte process motility and glutamatergic-dependent synaptic transmission. As autoantibodies directed against AQP4 are found in patients with the demyelinating autoimmune disease neuromyelitis optica (NMO-Ig) (Lennon et al., 2005) and strongly damage astrocyte functions through various immune mechanisms (Ratelade and Verkman,



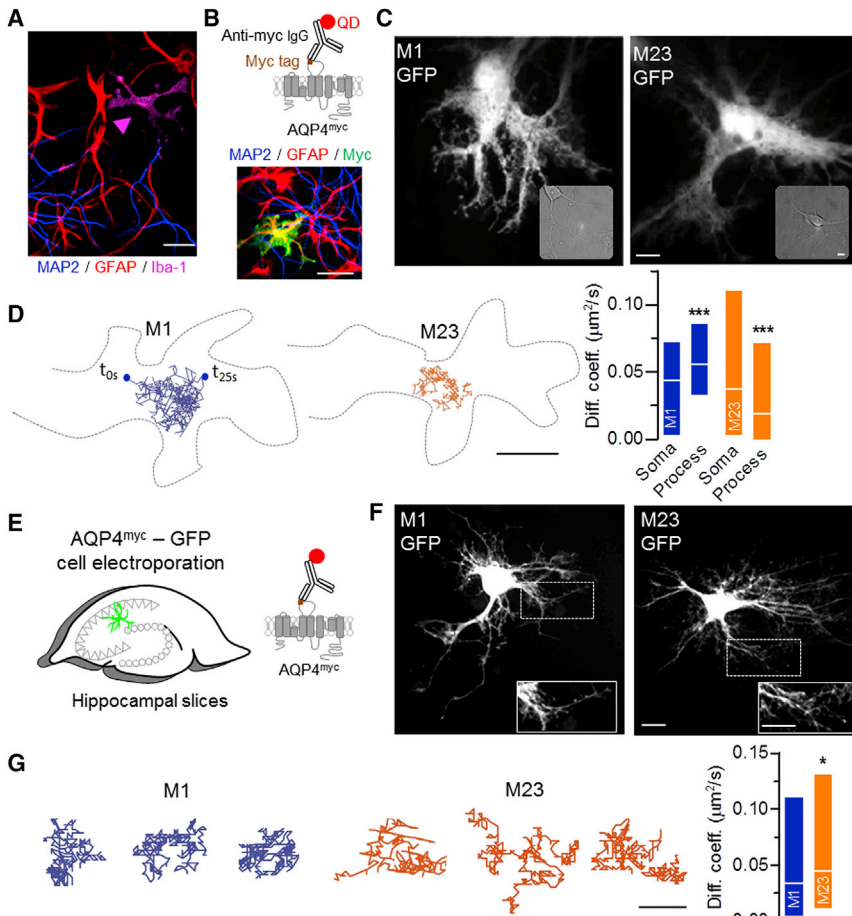


Figure 1. Surface Lateral of AQP4 Cluster in Hippocampal Mixed Culture and Slices

(A) Immunofluorescence showing mixed hippocampal cultures with astrocytes (red), neurons (blue), and microglia (arrowhead, magenta). Scale bar, 40 μm .

(B) Scheme of myc-tagged AQP4 (AQP4^{myc}) targeted by an anti-myc antibody (coupled to quantum dot [QD]). Bottom: immunostaining of MAP2 (neuronal dendrites), GFAP (glial cells), and Myc (transfected AQP4). Scale bar, 40 μm .

(C) Examples of astrocytes transfected with GFP and either AQP4-M1^{myc} or AQP4-M23^{myc}. Insets, DIC images of the corresponding mixed hippocampal cells. Scale bars (both images), 5 μm .

(D) Representative of AQP4-M1^{myc} and AQP4-M23^{myc} trajectories (~ 25 s duration) onto astrocyte processes. Right: instantaneous diffusion coefficients of AQP4-M1^{myc} (blue) and AQP4-M23^{myc} (orange) onto astrocyte soma ($n^{\text{AQP4-M1}} = 1,541$, $n^{\text{AQP4-M23}} = 2,200$ trajectories) and processes ($n^{\text{AQP4-M1}} = 1,405$, $n^{\text{AQP4-M23}} = 2,600$ trajectories). Scale bar, 0.5 μm .

(E) Schematic representation of hippocampal organotypic slice in which astrocytes have been electroporated with GFP and one AQP4^{myc} subtype. Right: scheme of myc-tagged AQP4 (AQP4^{myc}) targeted by an anti-myc antibody (coupled to quantum dot [QD]).

(F) Examples of astrocytes transfected with GFP and either AQP4-M1^{myc} or AQP4-M23^{myc}. Insets: enlarged astrocyte processes. Scale bars (both images), 5 μm .

(G) Three examples of AQP4-M1^{myc} (blue) and AQP4-M23^{myc} (orange) trajectories. Right: instantaneous diffusion coefficient of AQP4-M1^{myc} (M1) and AQP4-M23^{myc} (M23) ($n^{\text{AQP4-M1}} = 392$, $n^{\text{AQP4-M23}} = 340$ trajectories). Scale bar, 0.5 μm . In (D) and (G), data are presented as median \pm 25%–75% interquartile range (IQR) ($\mu\text{m}^2 \text{ s}^{-1}$) (* $p = 0.02$ and *** $p < 0.0001$, Mann-Whitney test).

2012), we investigated whether NMO-IgG perturbs AQP4 surface dynamics and distribution. Strikingly, AQP4 surface trafficking was strongly altered in the presence of NMO-IgG. The autoantibodies destabilized AQP4-M23 isoform, decreased astrocyte motility, and ultimately reduced NMDA receptor (NMDAR)-mediated synaptic activity. Altogether, we unveil a physiopathological interplay between astrocytic process motility and AQP4-M23 dynamics, shedding light on the regulatory molecular mechanisms underpinning the tripartite synapse.

RESULTS

Trafficking and Nanoscale Distribution of Surface AQP4 Isoforms in Hippocampal Cell Networks

The membrane trafficking of AQP4-M1 and AQP4-M23 was first measured in cultured hippocampal cells, composed of neurons, astrocytes, and microglia (Figure 1A), by imaging a single nanoparticle (quantum dot [QD]) coupled to one tagged AQP4 isoform (Figure 1B). Because the two isoforms (M1 and M23) have identical extracellular domains and thus cannot be distinguished with extracellular antibodies, a myc epitope was genetically inserted

into the second extracellular loop of AQP4-M1 and AQP4-M23, allowing specific live immunostaining and single-nanoparticle tracking (Figure 1B). Of note, the expression of AQP4^{myc} in astrocytes did not result in significant overexpression of the transporter (Figures S1A). The presence of the extracellular myc tag did not alter AQP4 water transport, measured by a gold-standard osmotic swelling assay (Madeira et al., 2016), in AQP4^{myc} transfected oocytes (Figure S1B). The use of tagged AQP4 and nanometer-size QD particles allowed us to track AQP4 complexes located at the surface of identified astrocytes. During our 30 min imaging experiments, the vast majority of tagged AQP4 was at the surface of astrocytes, as only few AQP4-QDs were detected inside astrocyte after acid wash treatment (Figure S1C) (Tardin et al., 2003). First, we compared the surface dynamics of AQP4-M1 and AQP4-M23 in the somatic and process compartments of highly polarized astrocytes (Figure 1C). AQP4-M1 diffusion was higher in processes compared with the somatic compartment (Figure 1D), whereas AQP4-M23 diffusion was lower in processes (Figure 1D). This indicates that the membrane trafficking of AQP4-M1 and AQP4-M23 is different onto astrocytes embedded into spontaneously active neuronal networks.

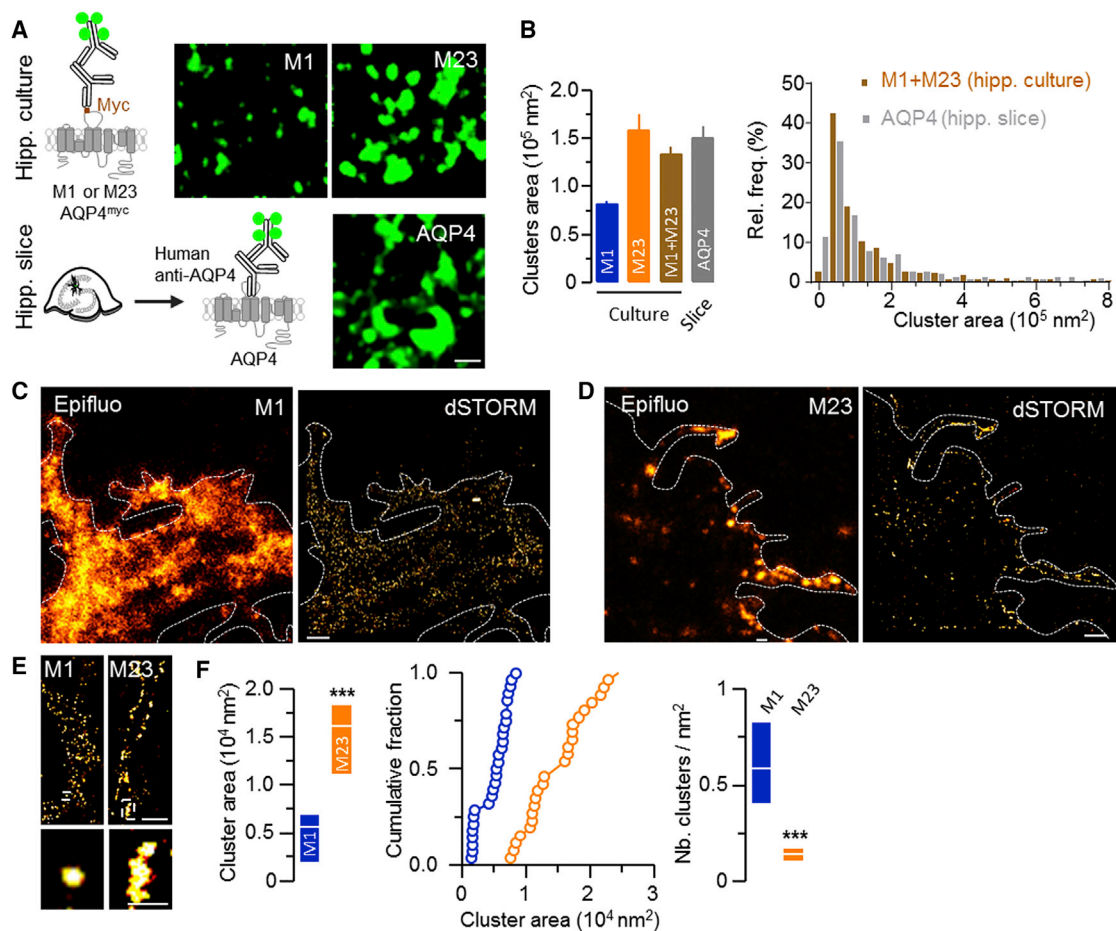


Figure 2. AQP4 Cluster Organization and Nanoscale Distribution in Hippocampal Organotypic Slices and Mixed Cultures

(A) Schematic representation of cultured astrocyte expressing myc-tagged AQP4 (AQP4^{myc}) targeted by an anti-myc antibody (coupled to organic fluorophores) and astrocyte from hippocampal slice expressing endogenous AQP4 (stained with NMO antibodies). Right: immunostaining of surface AQP4 clusters in mixed culture (top) and slice (bottom). Scale bar, 200 nm.

(B) Comparison of AQP4 cluster area between conditions. Right: distributions of AQP4 cluster areas between hippocampal cultures (brown) and slices (gray) (n = 20 regions for each condition).

(C and D) Wide-field (left) and dSTORM (right) images of astrocytes transfected with AQP4-M1^{myc} (C) or AQP4-M23^{myc} (D). Dotted lines represent the border of astrocytes on the basis of GFP epifluorescence images. Scale bars, 10 μ m.

(E) dSTORM magnified images of surface AQP4^{myc} subtype clusters onto astrocytic processes (top) and individual clusters (bottom). Scale bars, 2.5 μ m (top) and 100 nm (bottom).

(F) Comparison of AQP4-M1^{myc} (blue) and AQP4-M23^{myc} (orange) cluster area from dSTORM images (median \pm IQR). Right: normalized number of AQP4^{myc} clusters (n = 24 regions).

In (B), data are presented as mean $\times 10^5 \pm$ SEM (p = 0.12, one-way ANOVA). In (F), data are presented as median $\times 10^4 \pm$ IQR and median $\times 10^{-2} \pm$ IQR (nm²) (**p < 0.0001, Mann-Whitney test).

As astrocytes from primary cultures and brain slices differ in their morphology, which may influence trafficking of membrane proteins, we performed single-QD tracking of AQP4 isoforms on astrocytes within hippocampal organotypic slices, as previously pioneered on astrocytes with another transporter (Al Awabdh et al., 2016) and in neurons (Varela et al., 2016a, 2016b). The AQP4^{myc} isoforms and GFP were electroporated in astrocytes from hippocampal slices, and single-QD detection and tracking in organotypic slices was performed (Figures 1E and 1F), as recently described (Varela et al., 2016a, 2016b). Both AQP4-M1 and AQP4-M23 diffuse in the plasma membrane of astrocytes in hippocampal slices, while exhibiting different dy-

namics distribution (Figure 1G). Thus, besides providing evidence of single-molecule dynamics of AQP4 in hippocampal brain slice, our data collectively indicate that exogenously expressed AQP4-M1 and AQP4-M23 isoforms have differential dynamics at the surface of hippocampal astrocytes.

We then investigated the surface organization of AQP4 isoforms from *ex vivo* and *in vitro* astrocytes. In slices, we took advantages of the human anti-AQP4 immunoglobulins from NMO patients, which recognize extracellular domains of AQP4 (irrespective of isoforms), as a mean to immunostain all membrane AQP4 whatever the isoform. This staining was then compared with that of each isoform from cultured astrocytes (Figures 2A and 2B). The

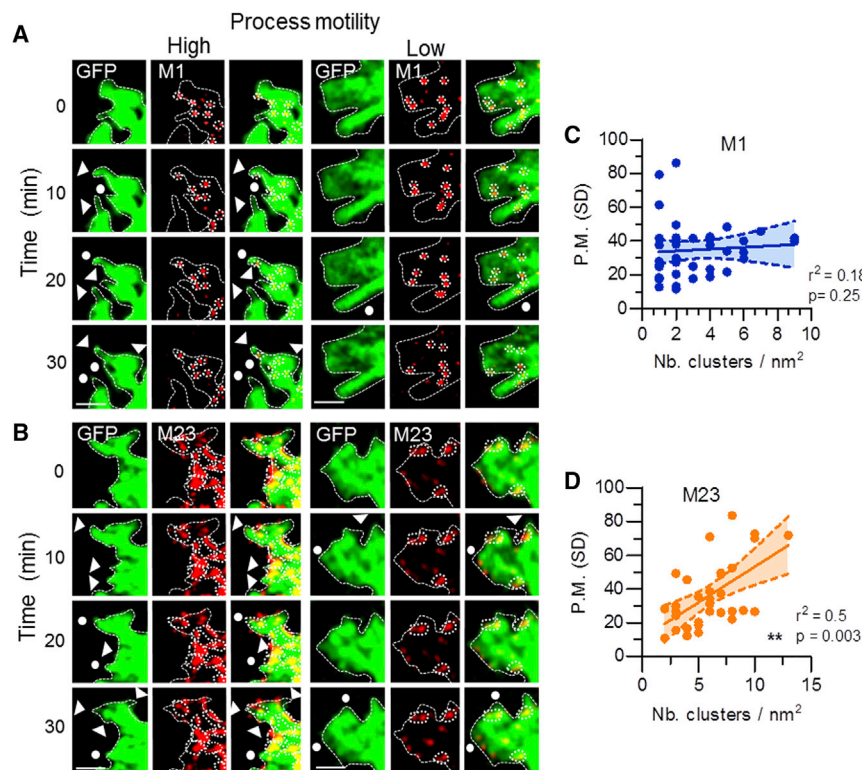


Figure 3. Correlation between Astrocyte Process Motility and AQP4 Isoform Content

(A and B) Time-lapse images of GFP-positive astrocyte processes in which surface AQP4-M1^{myc} (A) or AQP4-M23^{myc} (B) was labeled. White arrowheads highlight extension, and white circles highlight retraction. Dotted lines represent astrocyte borders. Scale bars, 2 μ m.

(C and D) Correlation between the number of clusters versus process motility (P.M.) (n = 40 astrocytes). Regression fit \pm SD is displayed. p = 0.25 (AQP4-M1; C) and **p = 0.003 (AQP4-M23; D) (Spearman correlation test). Analysis of astrocytic process motility can be found in Figure S2.

even distribution of small clusters, whereas AQP4-M23 slower dynamics would favor the formation of large clusters.

AQP4 Surface Trafficking Contributes to Astrocytic Process Motility in an Isoform-Dependent Manner

Whether the differential nanoscale organization and dynamics of AQP4-M1 and AQP4-M23 onto processes affect their functions, such as their motility, thus emerges as an intriguing possibility. First, we performed a time-lapse imaging for more than 30 min of astrocytic processes co-expressing GFP and either AQP4-M1 or AQP4-M23 and quantified the process motility (Figure S2). There was no correlation between the number of AQP4-M1 clusters onto the astrocyte processes and their motility (Figures 3A and 3C; $r^2 = 0.18$, p = 0.25). In contrast, processes with a larger number of AQP4-M23 displayed a higher motility, resulting in a significant positive correlation (Figures 3B and 3D; $r^2 = 0.5$, p = 0.003). The large AQP4-M23 clusters, but not AQP4-M1 ones, could thus have an instrumental role in the astrocytic process motility.

To experimentally address this possibility, we manipulated AQP4 dynamics by using a cross-linking (x-link) strategy (Dupuis et al., 2014; Groc et al., 2008; Heine et al., 2008; Murphy-Royal et al., 2015). Schematically, AQP4 isoforms were immobilized at the cell surface with a high concentration (200 μ g/mL) of primary antibody directed against myc tag (Figure 4A). At first, we controlled that the x-link assay alters the surface trafficking of the targeted AQP4 subtypes without affecting their water transport function. *Xenopus* oocytes immersed into distilled water (hypotonic stress) quickly swelled and lysed when expressing AQP4, a process prevented by the presence of AQP4 inhibitors (Igarashi et al., 2011; Migliati et al., 2009) (Figures 4B and S3A). The swelling, which is due to water movement through AQP4, was not altered by the high concentration of antibodies used for x-link (Figures 4B and S3A), indicating that AQP4-M23 function remained intact in this condition. As expected, the surface trafficking of AQP4-M23 was strongly reduced by the x-link procedure, increasing the size of existing clusters (Figures 3D and 4C). What then was the impact of this artificial alteration of

average cluster area of surface AQP4 from hippocampal slices was similar to that of AQP4-M1 and AQP4-M23 together (Figures 2A and 2B), indicating that the surface organization of AQP4 does not significantly differ between astrocytes from dissociated culture and brain slice. Yet it has been previously shown that AQP4-M1 and AQP4-M23 are differentially organized (Furman et al., 2003; Smith and Verkman, 2015; Smith et al., 2014). In order to map more specifically surface AQP4-M1 and AQP4-M23 on astrocytes, we used both classical confocal microscopy and the single-molecule localization microscopy technique of direct stochastic optical reconstruction microscopy (dSTORM) (Heilemann et al., 2008) to provide the nanoscale architecture of these two membrane proteins. First, diffraction-limited confocal imaging showed that AQP4-M1 forms surface clusters that are smaller than AQP4-M23 ones (Figures 2A and 2B) and revealed distinct distributions between AQP4-M1 and AQP4-M23 (Figures 2C and 2D). Noteworthy, we immunostained fixed astrocytes with anti-myc antibody to confirm that the 30 min incubation in live astrocytes did not induce clustering of surface AQP4 (Figure S1D). dSTORM imaging confirmed that at the nanoscale level, the organization of surface AQP4 subtypes is different, with a diffuse and uniform distribution of AQP4-M1 and a non-uniform distribution of AQP4-M23 with large clusters preferentially located at the edges of astrocyte processes (Figures 2C–2F). Consistently, AQP4-M1 clusters are more frequent, and smaller, than AQP4-M23 (Figure 2F). Thus, these data indicate that although both isoforms dynamically explore the astrocyte surface, their trafficking properties differ according to the astrocytic domains, fueling a model in which AQP4-M1 fast dynamics in processes are associated with an

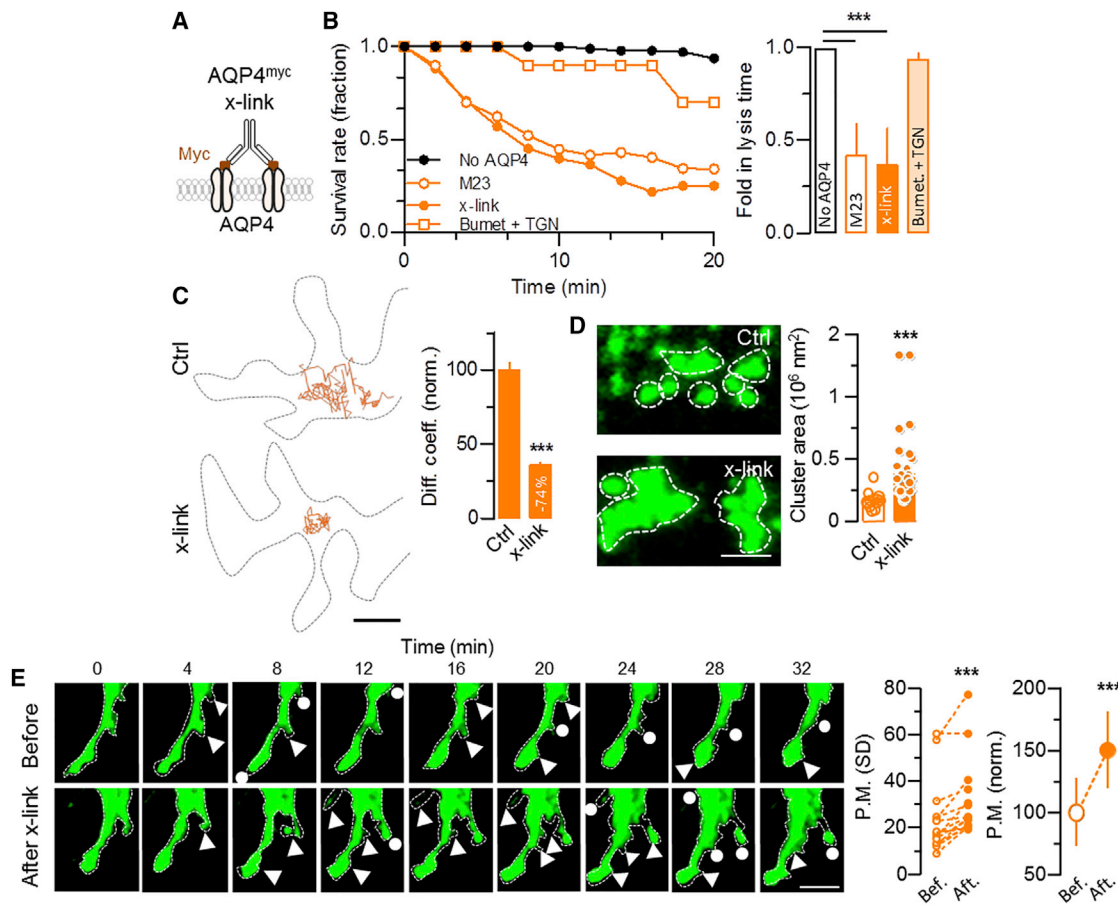


Figure 4. Immobilization of AQP4-M23 Affects Surface Cluster Size and Astrocytic Motility

(A) Schematic representation of myc-tagged AQP4 (AQP4^{myc}) that were x-linked through anti-myc antibodies. (B) Survival rate of oocytes expressing either no AQP4 (unrelated plasmid) or AQP4-M23^{myc} over time (left) and after 20 min (right) of exposure to x-link antibodies or the AQP4 inhibitors bumetanide (75 μ M) and TGN-020 (500 μ M) (n = 60 oocytes injected for each condition). (C) Representative AQP4-M23 trajectories in control and x-link conditions. Right: normalized instantaneous diffusion coefficient in control and x-link conditions (control [Ctrl], n = 697; x-link, n = 632 trajectories). Scale bar, 0.5 μ m. (D) Immunostaining (left) and comparison (right) of surface AQP4-M23 cluster size in control and x-link conditions (n = 30 regions for each condition). Scale bar, 200 nm. (E) Time-lapse imaging of GFP-expressing astrocytes before and after exposure to AQP4-M23 x-link. White arrowheads highlight extension, and white circles highlight retraction. Right: comparison of process motility (P.M.) calculated for individual process (n = 185 regions from 14 astrocytes; ***p < 0.0001, Mann-Whitney test). Scale bar, 2 μ m. In (B) and (C), data are represented as mean \pm SEM (***p < 0.0001, one-way ANOVA, and ***p < 0.0001, Mann-Whitney test, respectively). Data are represented in (D) as mean \times 10⁶ \pm SEM (***p < 0.0001, Mann-Whitney test).

AQP4-M23 dynamics and distribution on the astrocyte process motility? Remarkably, AQP4-M23 x-link significantly increased astrocytic process motility by 50% (Figure 4E), indicating that AQP4-M23 dynamic organization at the surface of astrocytes affects their process motility. Regarding AQP4-M1, their x-linking induced the formation of large clusters never observed in basal conditions (Figure S3). Then we investigated the impact of these artificially created AQP4-M1 clusters on process motility, with the reasoning that the creation of large clusters, like those naturally observed with AQP4-M23, may be sufficient to favor process motility, irrespective of the AQP4 subtype. However, the AQP4-M1 x-link decreased astrocyte process motility (Figure S3E), suggesting that the non-clustered distribution of

AQP4-M1 in steady-state conditions possibly contributes to the basal motility of processes and that AQP4-M23 dynamic and clustering has a specific role in regulating astrocyte process motility.

Neuronal Activity Bi-directionally Regulates AQP4 Surface Trafficking and Astrocytic Process Motility

Given that the neuronal activity regulates astrocytic process motility (Bernardinelli et al., 2014; Perez-Alvarez et al., 2014), we explored the possibility that AQP4 dynamics and distribution, especially those of AQP4-M23, are sensitive to neuronal network firing and contribute to the neuron-astrocyte cross-talk. First, AQP4 isoform dynamics were evaluated in the

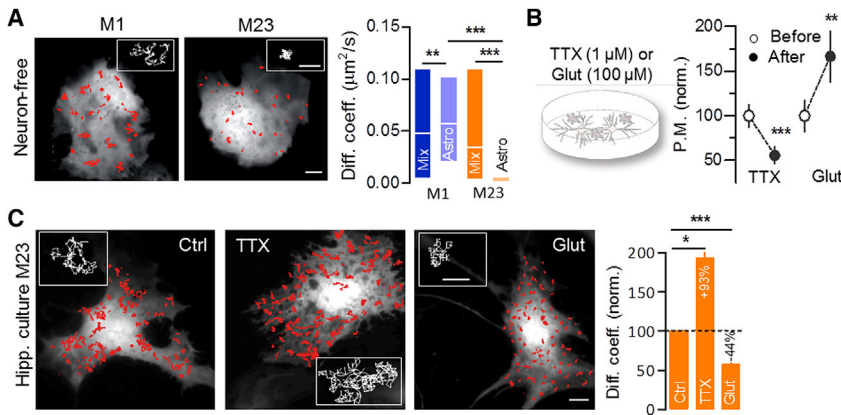


Figure 5. Activity-Dependent Regulation of AQP4 Surface Diffusion and Astrocytic Motility

(A) Trajectories of AQP4-M1^{myc} or AQP4-M23^{myc} onto neuron-free astrocyte culture. Scale bars, 5 μm and 0.5 μm (insets). Right: comparison of instantaneous diffusion coefficients of AQP4-M1^{myc} or AQP4-M23^{myc} trajectories (pure astrocyte [astro]; M1^{astro}, n = 833; M1^{mixed}, n = 4,400; M23^{astro}, n = 737; M23^{mix}, n = 6,200 trajectories).

(B) Mixed hippocampal cultures were exposed to TTX (1 μM) or glutamate (100 μM) for 20 min. Normalized process motility (P.M.) before and after application of TTX or glutamate (n^{TTX} = 22, n^{Glut} = 24 astrocytes).

(C) Trajectories of AQP4-M23^{myc} onto GFP-expressing astrocytes from mixed hippocampal cultures exposed to TTX (1 μM) or glutamate (100 μM) for 20 min. Insets: enlarged representative trajectories. Right: comparison of the normalized instantaneous

diffusion coefficients between conditions (n^{ctrl} = 500, n^{TTX} = 501, n^{Glut} = 584 trajectories). Scale bars, 5 μm and 0.5 μm (insets).

Data are presented in (A) as median \pm IQR (**p = 0.006 and ***p < 0.0001, one-way ANOVA), in (B) as SD (**p = 0.004 and ***p < 0.0001, Mann-Whitney test), and in (C) as mean \pm SEM (*p = 0.02, 0.015, and ***p < 0.0001, one-way ANOVA).

non-physiological condition with only astrocytes (neuron free). Strikingly, surface AQP4-M23 was nearly immobile, whereas the AQP4-M1 diffusion coefficient was only slightly affected compared with mixed glio-neuronal network condition (Figures 5A and S4A). These observations in pure cultured astrocytes, which display a balloon-like shape with virtually no process, suggest that AQP4-M23 trafficking is highly sensitive to the presence of neurons, neuronal activity, and/or astrocyte processes. Next, mixed hippocampal cultured networks were exposed to either 1 μM tetrodotoxin (TTX; a voltage-gated sodium channel blocker) to prevent action potential and repress neuronal firing, or to 100 μM glutamate to depolarize neurons and increase neuronal firing. As previously reported (Rusakov, 2015), we confirmed that astrocytic process motility decreased in the presence of TTX and, inversely, increased in the presence of glutamate (Figures 5B and S4B). As expected from the correlation between AQP4-M23 dynamic distribution and process motility, TTX and glutamate applications bi-directionally regulated AQP4-M23 surface trafficking. In TTX-silenced neuronal networks, the downregulation of process motility was associated with an increase in AQP4-M23 trafficking (Figure 5C). In the glutamate condition, the upregulation of process motility was associated with a decrease in AQP4-M23 trafficking (Figure 5C). The dynamics of AQP4-M1 were also sensitive to changes in neuronal activity (Figure S4C) but to a lesser extent compared with AQP4-M23 (Figure S4C). Collectively, these results indicate that AQP4-M23 trafficking is highly sensitive to neuronal activity, further supporting an instrumental role of AQP4-M23 dynamic distribution in the activity-dependent regulation of astrocytic process motility.

AQP4M23 Dynamics Near Glutamate Synapse Regulate Astrocyte Motility and Synaptic Events

The structural plasticity of astrocytic processes plays an important role in the development and physiology of the glutamate synapse, mostly through changes in the astrocytic coverage of pre- and postsynaptic compartments (Araque et al., 1999; Reichenbach et al., 2010; Ventura and Harris, 1999; Volterra

and Meldolesi, 2005). Consistent with the presence of a dynamic interplay between synapses and astrocytes, we observed that astrocytic process motility was higher near presynaptic terminals labeled with FM4-64 dye (Figure 6A). As AQP4-M23 surface clusters are important for astrocytic process motility, we tested whether AQP4-M23 organization regulates the glutamatergic basal synaptic transmission. First, immunostaining of surface AQP4-M1 and AQP4-M23 with the postsynaptic protein Homer 1c revealed that AQP4-M23 clusters were enriched onto astrocytic processes near glutamate synapses (Figure 6B). Consistently, membrane AQP4-M23 were trapped near synapses, as demonstrated by their reduced diffusion coefficient and increased dwell time in this compartment (Figures 6C and 6E). In contrast, AQP4-M1 was neither enriched nor retained near synapses (Figures 6B, 6D, and 6E). Then, to directly test whether AQP4-M23 organization on astrocyte process regulates the glutamate synapse transmission, AQP4-M23 was x-linked onto astrocytes while measuring spontaneous NMDAR-mediated calcium transients (isolated in presence of bicuculline, nifedipine, and Mg²⁺ free) into adjacent dendritic protrusions. Schematically, hippocampal neurons were transfected with the genetically encoded Ca²⁺ indicator GCaMP3, and astrocytes were transfected with AQP4-M23^{myc} (or AQP4-M1^{myc}; see STAR Methods). Expectedly, the addition of the NMDAR competitive antagonist APV (50 μM) completely abolished the calcium events, indicating that these events are mediated by NMDARs. Strikingly, NMDAR-mediated calcium transients were significantly more frequent in protrusions near AQP4-M23 x-link-induced high astrocytic process motility (Figure 6F), indicating that alterations of the AQP4-M23 dynamic organization and subsequent increased process motility are translated to the neighboring synapses. The NMDAR-mediated calcium transients were unaltered in protrusions near astrocytic processes in which AQP4-M1 dynamics were abolished (Figure 6F). Altogether, these data reveal that the dynamics and organization of AQP4-M23, but not of AQP4-M1, affect basal spontaneous synaptic transmission, most likely through the regulation of astrocytic process motility.

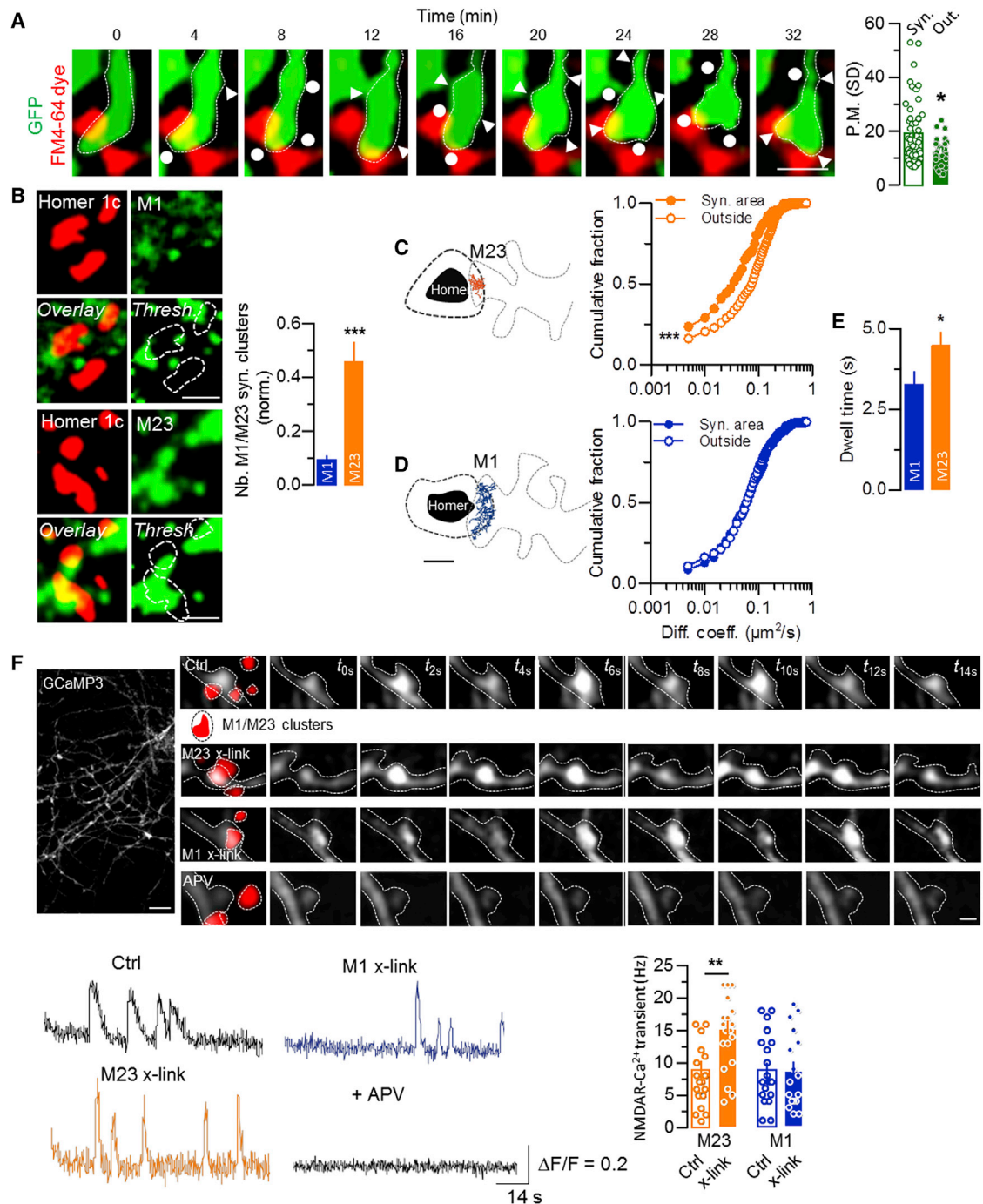


Figure 6. AQP4-M23 Aggregates around Synapses and Tunes Locally Astrocytic Motility

(A) Time-lapse images of GFP-expressing astrocyte processes depicting movements near activated synapse (labeled with FM4-64 dye). White arrowheads highlight extension, and white circles highlight retraction. Process motility (P.M.) of astrocyte processes surrounding (synaptic [syn.]) or away (outside [out.]) synapses (syn., $n = 54$; out., $n = 50$). Scale bar, 250 nm.

(B) Confocal microscopy images of surface AQP4-M1^{myc} or AQP4-M23^{myc} and postsynaptic density protein of glutamatergic synapses (Homer 1c). Normalized number of synaptic AQP4-M1^{myc} or AQP4-M23^{myc} clusters in the vicinity of glutamatergic synapses ($n = 20$ regions). Scale bar, 1 μ m.

(C and D) Representative AQP4-M23^{myc} (C, orange) and AQP4-M1^{myc} (D, blue) trajectories near glutamatergic synapses (Homer 1c). The perisynaptic areas (dotted line) correspond to 500 nm distance. Right: cumulative distributions inside and outside synaptic areas (AQP4-M23: $n^{\text{syn.}} = 178$, $n^{\text{out.}} = 820$; AQP4-M1: $n^{\text{syn.}} = 117$, $n^{\text{out.}} = 503$ trajectories). Scale bar, 0.5 μ m.

(E) Dwell time of AQP4-M1^{myc} (blue) and AQP4-M23^{myc} (orange) trajectories near synapses ($n^{\text{AQP4M1}} = 117$, $n^{\text{AQP4M23}} = 178$).

(legend continued on next page)

NMO Autoantibodies Modify Synaptic Transmission through Alteration of AQP4 Trafficking

Although the above antibody-induced alterations of AQP4 membrane distribution are artificial, autoantibodies directed against extracellular epitopes of AQP4 have been characterized in patients with NMO (Hinson et al., 2008, 2012; Marignier et al., 2010, 2016; Ratelade and Verkman, 2012; Ratelade et al., 2011; Rossi et al., 2012). These autoantibodies induce major dysfunctions of brain cell circuits, associated with severe clinical symptoms. To test whether the molecular mechanism by which these autoantibodies impair AQP4 function also involves alteration of water transporter dynamics and distribution on astrocytes, we purified NMO-IgG from three NMO patients who tested strongly positive for AQP4 IgG (Figure 7A). First, we evaluate whether NMO autoantibodies act as blockers of AQP4 function. For this, oocytes expressing AQP4-M23^{myc} or AQP4-M1^{myc} were exposed to serum containing NMO-IgG for 30 min and then immersed in hypotonic solution. NMO-IgG does not appear to alter water transport, as cell lysis of oocytes expressing AQP4-M23^{myc} or AQP4-M1^{myc} exposed to NMO-IgG was comparable with that of oocytes transfected alone or exposed to control (non-specific) IgG (Figure 7B). We next tested whether NMO-IgG alters the dynamics and distribution of AQP4 subtypes. Strikingly, when hippocampal networks were exposed to NMO-IgG (30 min), AQP4-M23 surface trafficking was increased as a result of disorganization of AQP4-M23 clusters whose size consistently decreased (Figures 7C and 7E). On the other hand, AQP4-M1 surface trafficking was decreased as a result of an aggregation of AQP4-M1 clusters that consistently increased (Figures 7D and 7E). Exposure of hippocampal networks to NMO-IgG therefore affected the surface trafficking of both AQP4 subtypes. On the basis of the above data, one would then predict that astrocytic process motility and synaptic NMDAR-mediated events will be decreased in hippocampal networks exposed to NMO-IgG. Consistently, NMO-IgG incubation decreased astrocyte process motility by approximately 50% (Figures 7F and S5A) whereas exposure to control IgG had no impact (Figure S5B). As NMO-IgG targets both isoforms, we controlled that exposing astrocytes expressing either AQP4-M1^{myc} or AQP4-M23^{myc} to NMO-IgG produced similar outcomes (Figure S5A). At the synaptic level, the frequency of synaptic NMDAR-mediated Ca²⁺ transients was significantly reduced in NMO-IgG-exposed neurons (Figure 7G). Collectively, these data indicate that acute exposure to NMO-IgG from patients strongly alters AQP4 surface dynamics, without affecting its function. The surface re-organization of AQP4 isoforms led to functional alteration of astrocyte process motility and basal synaptic transmission. On the basis of the key role of AQP4-M23 dy-

namics on the excitatory synaptic transmission, the NMO-IgG would thus likely affect the astrocyte-neuron interplay through their action on AQP4-M23 membrane distribution.

DISCUSSION

Using a combination of super-resolution, single-molecule, and calcium imaging approaches, we here demonstrate that the surface dynamics and nanoscale organization of AQP4-M23 onto astrocytic process regulate their motility and tune the basal transmission at glutamatergic synapses. Furthermore, the dynamic organization of AQP4-M23 is bi-directionally regulated by neuronal activity, supporting the presence of functional interplay between astrocytic motility and neuronal network activity. Autoantibodies directed against AQP4 from NMO patients alter the AQP4 surface dynamics, leaving intact their function. As a consequence, these autoantibodies impair the AQP4-dependent astrocytic process motility and basal transmission of glutamatergic synapses, consistent with the major defect of neuronal network in this disorder (Marignier et al., 2010, 2016). Although the molecular mechanisms underlying the regulation AQP4-M23 in these conditions remain enigmatic, these data fuel a model in which the membrane redistribution of AQP4-M23 in nanoscale clusters favors the rapid adaptation of astrocytic process volume and motility, affecting the basal transmission of glutamatergic synapses.

Astrocytic processes are thin and highly motile structures that respond to synaptic activity and long-term synaptic plasticity (Bernardinelli et al., 2014; Oliet et al., 2001; Perez-Alvarez et al., 2014). For instance, high synaptic activity is associated with a transient decrease in the extracellular space surrounding synapses (Dietzel et al., 1980), often related to the swelling of astrocyte processes. Indeed, an increase in synaptic activity increases the extracellular concentration of glutamate and potassium, whose clearance from the synaptic cleft requires astrocyte water influx through AQP4 (Haj-Yasein et al., 2012; Nagelhus and Ottersen, 2013). Currently, the structural adaptations of astrocyte processes are envisioned to be mediated by swelling-shrinking through water fluxes (Reichenbach et al., 2010) and actin-dependent mechanism (Haber et al., 2006). For instance, actin-depolymerizing molecules alter chloride and ionotropic fluxes at the plasma membrane, leading to morphological adaptations comparable with those observed in hypo-osmotic conditions (Lascola et al., 1998). Furthermore, swelling of perisynaptic glial processes through water intake causes transient rises in calcium that trigger actin depolymerization (Newman, 2001). Thus, water- and actin-dependent mechanisms likely work synergistically to tune the astrocyte process swelling and motility (Saadoun et al., 2005). We now report that the local regulation

(F) Representative time-lapse images (~14 s duration) of spontaneous synaptic NMDAR-mediated Ca²⁺ transients in basal condition and after AQP4-M23 or AQP4-M1 x-link. Surface AQP4-M1 or AQP4-M23 clusters are highlighted in red. Note that the NMDAR antagonist APV (50 μM) fully blocks spontaneous synaptic NMDAR-mediated Ca²⁺ transients. Scale bars, 20 μm and 2 μm (enlarged transients). Lower panel: fluorescence versus time trace of spontaneous synaptic NMDAR-mediated Ca²⁺ transients in control (Ctrl), AQP4-M1, or AQP4-M23 immobilization by x-link and in the presence of APV (50 μM). Right: comparison of NMDAR-mediated Ca²⁺ transient frequency (M23^{ctrl}, n = 21; M23^{x-link}, n = 21; M1^{ctrl}, n = 21; M1^{x-link}, n = 17 protrusions). The calcium fluorescent change is calculated from the ratio ΔF/F.

Data are presented in (A) as SD (*p = 0.02, Mann-Whitney test) and in (B) as mean ± SEM (**p < 0.0001, Mann-Whitney test). In (C) and (D), ***p < 0.0001 (Mann-Whitney test). Data are presented in (E) as mean ± SEM (*p = 0.04, Mann-Whitney test) and in (F) as mean ± SEM (**p = 0.0026, Student's t test).

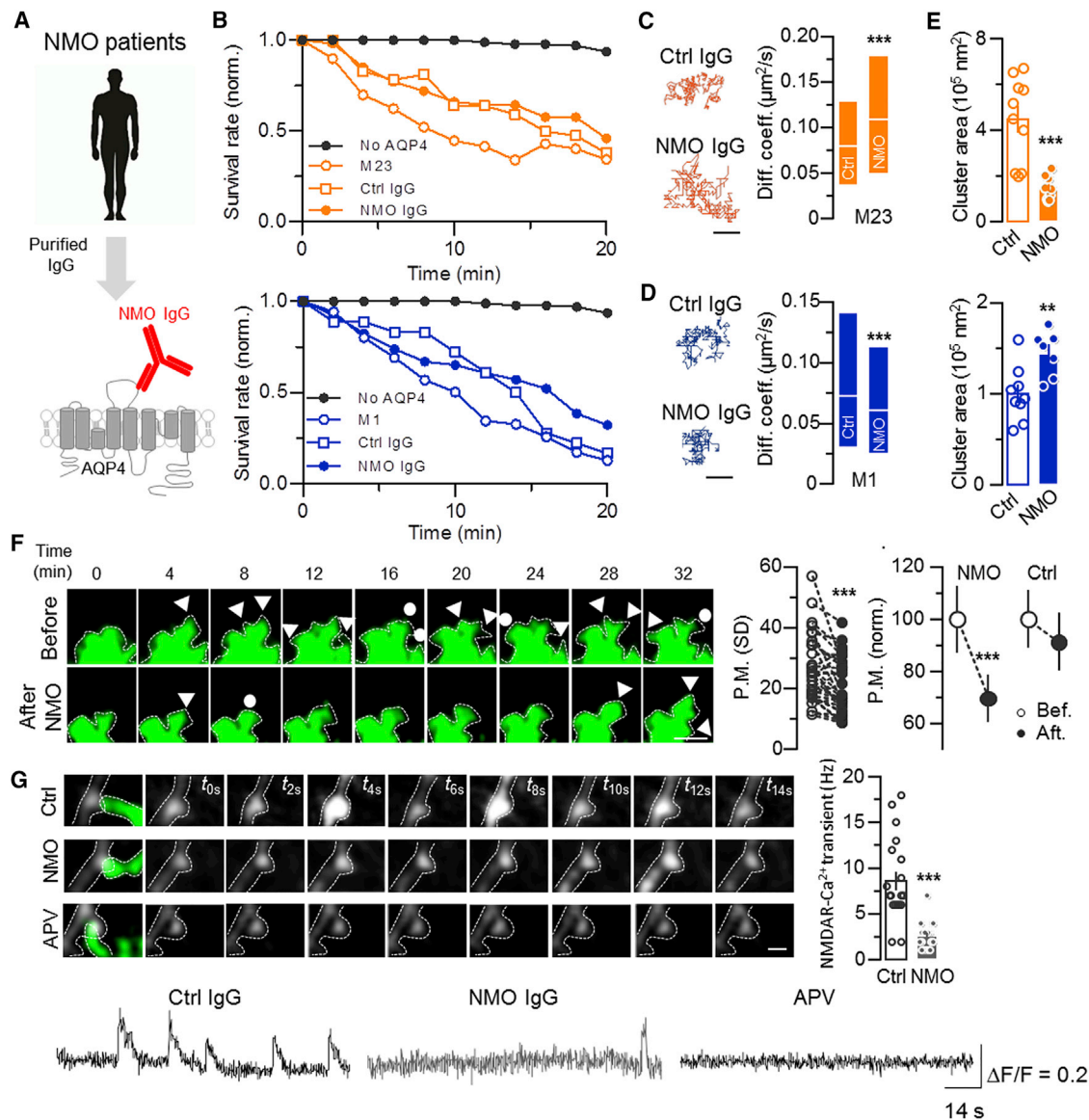


Figure 7. NMO-IgG Alters AQP4 Surface Diffusion, Astrocytic Motility, and Synaptic Activity

(A) IgG from NMO patients was purified and used to label surface AQP4.

(B) Survival rates of oocytes expressing no AQP4, AQP4-M1^{myc} (M1), or AQP4-M23^{myc} (M23) and exposed to control (Ctrl IgG) or NMO IgGs (n = 60 oocytes injected for each condition; no statistical difference between IgG conditions, one-way ANOVA).

(C) Representative trajectories of AQP4-M23^{myc} onto astrocytes exposed to control or NMO IgGs. Right: comparison of the instantaneous diffusion coefficients between conditions (AQP4-M23: n_{ctrl} = 1,300, n_{NMO} = 2,000 trajectories; ***p < 0.0001, Mann-Whitney test). Scale bars, 0.5 μm .

(D) Representative trajectories of AQP4-M1^{myc} onto astrocytes exposed to control or NMO IgGs. Right: comparison of the instantaneous diffusion coefficients between conditions (AQP4-M1: n_{ctrl} = 1,547, n_{NMO} = 2,882 trajectories; ***p < 0.0001, Mann-Whitney test). Scale bars, 0.5 μm .

(E) Effect of NMO IgG on AQP4-M23^{myc} (orange) and AQP4-M1^{myc} (blue) cluster area (n_{AQP4-M23} = 10, n_{AQP4-M1} = 9 astrocytes; **p = 0.003 and ***p < 0.0001, Mann-Whitney test).

(F) Time-lapse imaging of GFP-expressing astrocyte processes before and after NMO IgG incubation. Arrowheads highlight extension, and circles highlight retraction. Quantification of process motility (P.M.) from individual process (n_{NMO} = 170, n_{Ctrl} = 130 regions from 12 astrocytes). Scale bar, 2 μm .

(G) Time-lapse imaging of spontaneous synaptic NMDAR-mediated Ca^{2+} transients in the presence of control or NMO IgGs. Right: comparison of NMDAR-mediated Ca^{2+} transient frequency between conditions (mean \pm SEM; Ctrl IgG, n = 20; NMO IgG, n = 20 spines; ***p < 0.0001, Student's t test). The calcium fluorescent change is calculated from the ratio $\Delta F/F$. Scale bar, 2 μm .

Data are presented in (C) and (D) as median \pm IQR, in (E) as mean $\times 10^5 \pm$ SEM, and in (F) as SD.

of the water transporter AQP4-M23 in astrocytic processes is instrumental in tuning process motility. Although both AQP4-M1 and AQP4-M23 diffuse at the surface of astrocytic processes, like other membrane proteins in astrocytes (Arizono et al., 2012; Murphy-Royal et al., 2015; Al Awabdh et al., 2016), important differences between isoforms were unveiled. For instance, AQP4-M1 was highly dynamic and homogeneously distributed into small nanoscale clusters, whereas AQP4-M23 slowly diffuses and aggregates into large clusters on motile processes. Interestingly, the presence of neurons and the neuronal activity tune the surface dynamics of AQP4-M23, consistent with former reports in pure astrocyte preparations (Crane et al., 2008, 2010). Thus, in both *in vitro* and *ex vivo* hippocampal networks, AQP4-M23 dynamics and nanoscale cluster organization reflect the status of the neuronal network activity and likely serve in the homeostatic regulation of the tripartite synapse. We acknowledge that the present data were collected solely in astrocytes from hippocampal cultures and organotypic slices, which may not fully capture the *in vivo* polarization of AQP4 distribution on astrocyte endfeet. Yet AQP4 subtypes were differentially organized, in agreement with the well-described larger AQP4-M23 assemblies (Crane et al., 2010). Furthermore, AQP4-M23 clusters with similar organization were previously described in the brain parenchyma; clusters that were significantly smaller compared with AQP4-M23 endfeet in perivascular areas (Smith and Verkman, 2015). Thus, the described surface dynamics and spatial distribution of AQP4-M23 are consistent with previous work and surely shed light on AQP4 regulation in brain networks.

Although the molecular mechanism underlying this regulation remains unknown, one may speculate that the activation of astrocytic metabotropic glutamate receptor and subsequent calcium-calmodulin-dependent protein kinase II (CaMKII) phosphorylate AQP4 (Gunnarson et al., 2005, 2008), a process known to strongly influence receptor and transporter surface dynamics (Battaglia et al., 2018; Carta et al., 2013; Folci et al., 2018; Gianone et al., 2013; Opazo et al., 2010; Schweitzer et al., 2017). Additionally, protein-protein interactions with scaffolding proteins (Choquet and Triller, 2013) or other transmembrane proteins, such as the Na⁺/K⁺ ATPase (Illarionova et al., 2010), can also play an important role in this process. As it has been recently shown that the astrocytic glutamate transporter GLT-1 is dynamically anchored near synapses (Murphy-Royal et al., 2015), the presence of macromolecular complexes containing glutamate and water transporters, as well as glutamate receptors, in this strategic location may serve as “sensing” and “plastic” entities, enabling the local adaptations of astrocytic processes with the synaptic activity.

The role of AQP4 in synaptic long-term plasticity, learning, and memory has been supported by several lines of evidence (Scharfman and Binder, 2013; Szu and Binder, 2016; Wu et al., 2017; Yang et al., 2013). For instance, mice in which the AQP4 gene has been knocked out display impaired NMDAR-dependent long-term potentiation and depression at hippocampal glutamatergic synapses (Li et al., 2012). Moreover, changes in AQP4 expression have been associated with altered neuronal network acidity and neuronal excitability (Binder et al., 2012). How would a change in astrocytic AQP4 relate to NMDAR-

dependent alteration of the glutamate synapse? Together with our observations that AQP4-M23 nanoscale dynamics regulate astrocyte process motility and NMDAR-mediated synaptic events, we propose that AQP4 aggregation favors the astrocytic coverage of glutamate synapse, altering the concentration of glutamate in the synaptic cleft and its vicinity (Oliet et al., 2001; Theodosis and Poulain, 1993; Theodosis et al., 2008), as well as the release of gliotransmitters, such as D-serine, which are essential for NMDAR activation in hippocampal synapse (Henneberger et al., 2010; Panatier et al., 2006). Thus, activity-dependent changes in AQP4-M23 distribution on motile astrocytic processes can tune the recruitment of NMDAR signaling and, as a consequence, NMDAR-dependent plasticity processes. Our capability to alter the surface trafficking of AQP4 in a time-dependent manner is likely more sensitive than a total knockout approach (AQP4^{-/-}), for which compensations might explain that synaptic transmission has been found altered only after potentiation but not under basal conditions (Scharfman and Binder, 2013; Szu and Binder, 2016; Wu et al., 2017; Yang et al., 2013).

Finally, understanding how AQP4 is functionally organized and participates in the dialog between astrocytes and neurons is also a major challenge for clinics, as most patients with NMO spectrum disorder show autoantibodies targeting AQP4. Our data indicate that these autoantibodies are acutely deleterious by themselves (i.e., without cell or complement cytotoxicity), not because they block the water transport flux but because they displace membrane AQP4 isoforms and set a functional nanoscale organization that strongly restrains astrocyte process motility. Indeed, the binding of NMO-IgG to AQP4 bi-directionally modifies AQP4-M1 and AQP4-M23 surface diffusion. The consequences on astrocyte process motility and glutamate synapse transmission, which are significantly decreased, are well in line with what could be predicted on the basis of x-link manipulations. These alterations could also be combined with additional effects of NMO-IgG on the glutamate uptake from astrocytes and consequent glutamate excitotoxicity that have been involved in the pathogenesis of long-term exposure to NMO (Hinson et al., 2008; Marignier et al., 2010, 2016). This work thus provides direction for a molecular and cellular framework to better characterize the molecular dysregulation underpinning NMO spectrum disorders. Noteworthy, this “single-molecule” study of this autoimmune disease echoes, to some extent, recent investigations in which the impact of autoantibodies directed against the glutamatergic NMDAR and purified from patients with neuropsychiatric conditions has been identified (Jézéquel et al., 2017; Krugers et al., 2010; Mikasova et al., 2012). These studies unveiled that autoantibodies that target extracellular epitopes of the NMDAR do not alter its ionotropic function but displace the receptor from the postsynaptic density to the extrasynaptic membrane compartment in which the receptor is later endocytosed. Beyond a better understanding of the cellular and molecular mechanisms involved in autoimmune diseases of the CNS, such study has also opened avenues of research for innovative therapeutically strategies in which a balance of the dynamics and distribution of the autoantibody target is explored.

STAR★METHODS

Detailed methods are provided in the online version of this paper and include the following:

- **KEY RESOURCES TABLE**
- **LEAD CONTACT AND MATERIALS AVAILABILITY**
- **EXPERIMENTAL MODEL AND SUBJECT DETAILS**
 - Cell culture
 - Human sera and IgG purification
 - Organotypic slices
- **METHOD DETAILS**
 - Cell culture transfection
 - Immunohistochemistry
 - Organotypic slices electroporation
 - Quantum dots labeling and imaging
 - dSTORM and Image-based cluster analysis
 - Time-lapse imaging and analysis
 - Osmotic swelling assay
 - Calcium imaging and analysis
- **QUANTIFICATION AND STATISTICAL ANALYSIS**

SUPPLEMENTAL INFORMATION

Supplemental Information can be found online at <https://doi.org/10.1016/j.celrep.2019.05.097>.

ACKNOWLEDGMENTS

This work was supported by Centre National de la Recherche Scientifique, Agence Nationale de la Recherche, Fondation pour la Recherche Médicale, Conseil Régional d'Aquitaine, and French Agence Nationale de la Recherche within the context of the Laboratory of Excellence TRAIL program (referenced ANR-10-LABX-57 named TRAIL) (project IBIO-NI and GM-COG), Labex BRAIN, ARSEP Foundation, and Fondation pour l'Aide à la Recherche sur la Sclérose en Plaques. We thank the Bordeaux Imaging Center (service unit of CNRS-INSERM and Bordeaux University, member of the national infrastructure France Biolmaging) for confocal and STORM imaging. We thank Pauline Durand for technical assistance on molecular biology and lab members for constructive discussions.

AUTHOR CONTRIBUTIONS

S.C., D.B., N.D., B.K., C.M., and E.B.-G. performed the experiments. S.C., E.B.-G., and T.T. analyzed data. R.M. provided human samples. S.C., S.H.R.O., T.T., and L.G. conceived and designed the experiments.

DECLARATION OF INTERESTS

The authors declare no competing interests.

Received: September 28, 2018

Revised: March 8, 2019

Accepted: May 23, 2019

Published: June 25, 2019

REFERENCES

Al Awabdh, S., Gupta-Agarwal, S., Sheehan, D.F., Muir, J., Norkett, R., Twelvetrees, A.E., Griffin, L.D., and Kittler, J.T. (2016). Neuronal activity mediated regulation of glutamate transporter GLT-1 surface diffusion in rat astrocytes in dissociated and slice cultures. *Glia* 64, 1252–1264.

Amiry-Moghaddam, M., and Ottersen, O.P. (2003). The molecular basis of water transport in the brain. *Nat. Rev. Neurosci.* 4, 991–1001.

Araque, A., Parpura, V., Sanzgiri, R.P., and Haydon, P.G. (1999). Tripartite synapses: glia, the unacknowledged partner. *Trends Neurosci.* 22, 208–215.

Arizono, M., Bannai, H., Nakamura, K., Niwa, F., Enomoto, M., Matsu-Ura, T., Miyamoto, A., Sherwood, M.W., Nakamura, T., and Mikoshiba, K. (2012). Receptor-selective diffusion barrier enhances sensitivity of astrocytic processes to metabotropic glutamate receptor stimulation. *Sci. Signal.* 5, ra27.

Bard, L., Sainlos, M., Bouchet, D., Cousins, S., Mikasova, L., Breillat, C., Stephenson, F.A., Imperiali, B., Choquet, D., and Groc, L. (2010). Dynamic and specific interaction between synaptic NR2-NMDA receptor and PDZ proteins. *Proc. Natl. Acad. Sci. U S A* 107, 19561–19566.

Battaglia, S., Renner, M., Russeau, M., Côme, E., Tyagarajan, S.K., and Lévi, S. (2018). Activity-dependent inhibitory synapse scaling is determined by gephyrin phosphorylation and subsequent regulation of GABA A receptor diffusion. *eNeuro* 5, ENEURO.0203-17.2017.

Bernardinelli, Y., Randall, J., Janett, E., Nikonenko, I., König, S., Jones, E.V., Flores, C.E., Murai, K.K., Bochet, C.G., Holtmaat, A., and Müller, D. (2014). Activity-dependent structural plasticity of perisynaptic astrocytic domains promotes excitatory synapse stability. *Curr. Biol.* 24, 1679–1688.

Binder, D.K., Nagelhus, E.A., and Ottersen, O.P. (2012). Aquaporin-4 and epilepsy. *Glia* 60, 1203–1214.

Carta, M., Opazo, P., Veran, J., Athané, A., Choquet, D., Coussen, F., and Mülle, C. (2013). CaMKII-dependent phosphorylation of GluK5 mediates plasticity of kainate receptors. *EMBO J.* 32, 496–510.

Choquet, D., and Triller, A. (2013). The dynamic synapse. *Neuron* 80, 691–703.

Crane, J.M., Van Hoek, A.N., Skach, W.R., and Verkman, A.S. (2008). Aquaporin-4 dynamics in orthogonal arrays in live cells visualized by quantum dot single particle tracking. *Mol. Biol. Cell* 19, 3369–3378.

Crane, J.M., Tajima, M., and Verkman, A.S. (2010). Live-cell imaging of aquaporin-4 diffusion and interactions in orthogonal arrays of particles. *Neuroscience* 168, 892–902.

Dietzel, I., Heinemann, U., Hofmeier, G., and Lux, H.D. (1980). Transient changes in the size of the extracellular space in the sensorimotor cortex of cats in relation to stimulus-induced changes in potassium concentration. *Exp. Brain Res.* 40, 432–439.

Dupuis, J.P., Ladépêche, L., Seth, H., Bard, L., Varela, J., Mikasova, L., Bouchet, D., Rogemond, V., Honnorat, J., Hanse, E., and Groc, L. (2014). Surface dynamics of GluN2B-NMDA receptors controls plasticity of maturing glutamate synapses. *EMBO J.* 33, 842–861.

Folci, A., Steinberger, A., Lee, B., Stanika, R., Scheruebel, S., Campiglio, M., Ramprecht, C., Pelzmann, B., Hell, J.W., Obermair, G.J., et al. (2018). Molecular mimicking of C-terminal phosphorylation tunes the surface dynamics of Cav1.2 calcium channels in hippocampal neurons. *J. Biol. Chem.* 293, 1040–1053.

Furman, C.S., Gorelick-Feldman, D.A., Davidson, K.G.V., Yasumura, T., Neely, J.D., Agre, P., and Rash, J.E. (2003). Aquaporin-4 square array assembly: opposing actions of M1 and M23 isoforms. *Proc. Natl. Acad. Sci. U S A* 100, 13609–13614.

Giannone, G., Mondin, M., Grillo-Bosch, D., Tessier, B., Saint-Michel, E., Czöndör, K., Sainlos, M., Choquet, D., and Thoumine, O. (2013). Neurexin-1β binding to neuroligin-1 triggers the preferential recruitment of PSD-95 versus gephyrin through tyrosine phosphorylation of neuroligin-1. *Cell Rep.* 3, 1996–2007.

Groc, L., Heine, M., Cognet, L., Brickley, K., Stephenson, F.A., Lounis, B., and Choquet, D. (2004). Differential activity-dependent regulation of the lateral mobilities of AMPA and NMDA receptors. *Nat. Neurosci.* 7, 695–696.

Groc, L., Lafourcade, M., Heine, M., Renner, M., Racine, V., Sibarita, J.-B., Lounis, B., Choquet, D., and Cognet, L. (2007). Surface trafficking of neurotransmitter receptor: comparison between single-molecule/quantum dot strategies. *J. Neurosci.* 27, 12433–12437.

- Groc, L., Choquet, D., and Chaouloff, F. (2008). The stress hormone corticosterone conditions AMPAR surface trafficking and synaptic potentiation. *Nat. Neurosci.* *11*, 868–870.
- Gunnarson, E., Axehult, G., Baturina, G., Zelenin, S., Zelenina, M., and Aperia, A. (2005). Lead induces increased water permeability in astrocytes expressing aquaporin 4. *Neuroscience* *136*, 105–114.
- Gunnarson, E., Zelenina, M., Axehult, G., Song, Y., Bondar, A., Krieger, P., Brismar, H., Zelenin, S., and Aperia, A. (2008). Identification of a molecular target for glutamate regulation of astrocyte water permeability. *Glia* *56*, 587–596.
- Haber, M., Zhou, L., and Murai, K.K. (2006). Cooperative astrocyte and dendritic spine dynamics at hippocampal excitatory synapses. *J. Neurosci.* *26*, 8881–8891.
- Haj-Yasein, N.N., Jensen, V., Østby, I., Omholt, S.W., Voipio, J., Kaila, K., Ottersen, O.P., Hvalby, Ø., and Nagelhus, E.A. (2012). Aquaporin-4 regulates extracellular space volume dynamics during high-frequency synaptic stimulation: a gene deletion study in mouse hippocampus. *Glia* *60*, 867–874.
- Halassa, M.M., and Haydon, P.G. (2010). Integrated brain circuits: astrocytic networks modulate neuronal activity and behavior. *Annu. Rev. Physiol.* *72*, 335–355.
- Heilemann, M., van de Linde, S., Schüttelz, M., Kasper, R., Seefeldt, B., Mukherjee, A., Tinnefeld, P., and Sauer, M. (2008). Subdiffraction-resolution fluorescence imaging with conventional fluorescent probes. *Angew. Chem. Int. Ed. Engl.* *47*, 6172–6176.
- Heine, M., Groc, L., Frischknecht, R., Beique, J.-C., Lounis, B., Rumbaugh, G., Huganir, R.L., Cognet, L., and Choquet, D. (2008). Surface mobility of postsynaptic AMPARs tunes synaptic transmission. *Science* *320*, 201–205.
- Henneberger, C., Papouin, T., Oliet, S.H.R., and Rusakov, D.A. (2010). Long-term potentiation depends on release of D-serine from astrocytes. *Nature* *463*, 232–236.
- Hinson, S.R., Roemer, S.F., Lucchinetti, C.F., Fryer, J.P., Kryzer, T.J., Chamberlain, J.L., Howe, C.L., Pittock, S.J., and Lennon, V.A. (2008). Aquaporin-4 binding autoantibodies in patients with neuromyelitis optica impair glutamate transport by down-regulating EAAT2. *J. Exp. Med.* *205*, 2473–2481.
- Hinson, S.R., Romero, M.F., Popescu, B.F.G., Lucchinetti, C.F., Fryer, J.P., Wolburg, H., Fallier-Becker, P., Noell, S., and Lennon, V.A. (2012). Molecular outcomes of neuromyelitis optica (NMO)-IgG binding to aquaporin-4 in astrocytes. *Proc. Natl. Acad. Sci. U S A* *109*, 1245–1250.
- Igarashi, H., Huber, V.J., Tsujita, M., and Nakada, T. (2011). Pretreatment with a novel aquaporin 4 inhibitor, TGN-020, significantly reduces ischemic cerebral edema. *Neurol. Sci.* *32*, 113–116.
- Illarionova, N.B., Gunnarson, E., Li, Y., Brismar, H., Bondar, A., Zelenin, S., and Aperia, A. (2010). Functional and molecular interactions between aquaporins and Na,K-ATPase. *Neuroscience* *168*, 915–925.
- Jézéquel, J., Rogemond, V., Pollak, T., Lepieux, M., Jacobson, L., Gréa, H., Iyegbe, C., Kahn, R., McGuire, P., Vincent, A., et al. (2017). Cell- and single molecule-based methods to detect anti-N-methyl-D-aspartate receptor autoantibodies in patients with first-episode psychosis from the OPTIMISE project. *Biol. Psychiatry* *82*, 766–772.
- Jiang, M., and Chen, G. (2006). High Ca²⁺-phosphate transfection efficiency in low-density neuronal cultures. *Nat. Protoc.* *1*, 695–700.
- Jo, Y.-H., Donier, E., Martinez, A., Garret, M., Toulmé, E., and Boué-Grabot, E. (2011). Cross-talk between P2X₄ and γ -aminobutyric acid, type A receptors determines synaptic efficacy at a central synapse. *J. Biol. Chem.* *286*, 19993–20004.
- Kimelberg, H.K. (2004). Water homeostasis in the brain: basic concepts. *Neuroscience* *129*, 851–860.
- Krugers, H.J., Hoogenraad, C.C., and Groc, L. (2010). Stress hormones and AMPA receptor trafficking in synaptic plasticity and memory. *Nat. Rev. Neurosci.* *11*, 675–681.
- Lascola, C.D., Nelson, D.J., and Kraig, R.P. (1998). Cytoskeletal actin gates a Cl⁻ channel in neocortical astrocytes. *J. Neurosci.* *18*, 1679–1692.
- Lennon, V.A., Kryzer, T.J., Pittock, S.J., Verkman, A.S., and Hinson, S.R. (2005). IgG marker of optic-spinal multiple sclerosis binds to the aquaporin-4 water channel. *J. Exp. Med.* *202*, 473–477.
- Li, Y.-K., Wang, F., Wang, W., Luo, Y., Wu, P.-F., Xiao, J.-L., Hu, Z.-L., Jin, Y., Hu, G., and Chen, J.-G. (2012). Aquaporin-4 deficiency impairs synaptic plasticity and associative fear memory in the lateral amygdala: involvement of downregulation of glutamate transporter-1 expression. *Neuropsychopharmacology* *37*, 1867–1878.
- Madeira, A., Moura, T.F., and Soveral, G. (2016). Detecting aquaporin function and regulation. *Front Chem.* *4*, 3.
- Manley, G.T., Fujimura, M., Ma, T., Noshita, N., Filiz, F., Bollen, A.W., Chan, P., and Verkman, A.S. (2000). Aquaporin-4 deletion in mice reduces brain edema after acute water intoxication and ischemic stroke. *Nat. Med.* *6*, 159–163.
- Marignier, R., Nicolle, A., Watrin, C., Touret, M., Cavagna, S., Varrin-Doyer, M., Cavillon, G., Rogemond, V., Confavreux, C., Honnorat, J., and Giraudon, P. (2010). Oligodendrocytes are damaged by neuromyelitis optica immunoglobulin G via astrocyte injury. *Brain* *133*, 2578–2591.
- Marignier, R., Ruiz, A., Cavagna, S., Nicole, A., Watrin, C., Touret, M., Parrot, S., Malleret, G., Peyron, C., Benetollo, C., et al. (2016). Neuromyelitis optica study model based on chronic infusion of autoantibodies in rat cerebrospinal fluid. *J. Neuroinflammation* *13*, 111.
- Migliati, E., Meurice, N., DuBois, P., Fang, J.S., Somasekharan, S., Beckett, E., Flynn, G., and Yool, A.J. (2009). Inhibition of aquaporin-1 and aquaporin-4 water permeability by a derivative of the loop diuretic bumetanide acting at an internal pore-occluding binding site. *Mol. Pharmacol.* *76*, 105–112.
- Mikasova, L., De Rossi, P., Bouchet, D., Georges, F., Rogemond, V., Didelot, A., Meissirel, C., Honnorat, J., and Groc, L. (2012). Disrupted surface cross-talk between NMDA and Ephrin-B2 receptors in anti-NMDA encephalitis. *Brain* *135*, 1606–1621.
- Mongin, A.A., and Kimelberg, H.K. (2005). ATP regulates anion channel-mediated organic osmolyte release from cultured rat astrocytes via multiple Ca²⁺-sensitive mechanisms. *Am. J. Physiol. Cell Physiol.* *288*, C204–C213.
- Murphy-Royal, C., Dupuis, J.P., Varela, J.A., Panatier, A., Pinson, B., Baufreton, J., Groc, L., and Oliet, S.H.R. (2015). Surface diffusion of astrocytic glutamate transporters shapes synaptic transmission. *Nat. Neurosci.* *18*, 219–226.
- Nagelhus, E.A., and Ottersen, O.P. (2013). Physiological roles of aquaporin-4 in brain. *Physiol. Rev.* *93*, 1543–1562.
- Newman, E.A. (2001). Propagation of intercellular calcium waves in retinal astrocytes and Müller cells. *J. Neurosci.* *21*, 2215–2223.
- Oliet, S.H.R., Piet, R., and Poulain, D.A. (2001). Control of glutamate clearance and synaptic efficacy by glial coverage of neurons. *Science* *292*, 923–926.
- Opazo, P., Labrecque, S., Tigaret, C.M., Frouin, A., Wiseman, P.W., De Koninck, P., and Choquet, D. (2010). CaMKII triggers the diffusional trapping of surface AMPARs through phosphorylation of stargazin. *Neuron* *67*, 239–252.
- Panatier, A., Theodosis, D.T., Mothet, J.-P., Touquet, B., Pollegioni, L., Poulain, D.A., and Oliet, S.H.R. (2006). Glia-derived D-serine controls NMDA receptor activity and synaptic memory. *Cell* *125*, 775–784.
- Patel, T.P., Man, K., Firestein, B.L., and Meaney, D.F. (2015). Automated quantification of neuronal networks and single-cell calcium dynamics using calcium imaging. *J. Neurosci. Methods* *243*, 26–38.
- Perez-Alvarez, A., Navarrete, M., Covelo, A., Martin, E.D., and Araque, A. (2014). Structural and functional plasticity of astrocyte processes and dendritic spine interactions. *J. Neurosci.* *34*, 12738–12744.
- Ratelade, J., and Verkman, A.S. (2012). Neuromyelitis optica: aquaporin-4 based pathogenesis mechanisms and new therapies. *Int. J. Biochem. Cell Biol.* *44*, 1519–1530.
- Ratelade, J., Bennett, J.L., and Verkman, A.S. (2011). Evidence against cellular internalization *in vivo* of NMO-IgG, aquaporin-4, and excitatory amino acid transporter 2 in neuromyelitis optica. *J. Biol. Chem.* *286*, 45156–45164.
- Reichenbach, A., Derouiche, A., and Kirchhoff, F. (2010). Morphology and dynamics of perisynaptic glia. *Brain Res. Brain Res. Rev.* *63*, 11–25.

- Rossi, A., Ratelade, J., Papadopoulos, M.C., Bennett, J.L., and Verkman, A.S. (2012). Neuromyelitis optica IgG does not alter aquaporin-4 water permeability, plasma membrane M1/M23 isoform content, or supramolecular assembly. *Glia* 60, 2027–2039.
- Rusakov, D.A. (2015). Disentangling calcium-driven astrocyte physiology. *Nat. Rev. Neurosci.* 16, 226–233.
- Saadoun, S., Papadopoulos, M.C., Watanabe, H., Yan, D., Manley, G.T., and Verkman, A.S. (2005). Involvement of aquaporin-4 in astroglial cell migration and glial scar formation. *J. Cell Sci.* 118, 5691–5698.
- Scharfman, H.E., and Binder, D.K. (2013). Aquaporin-4 water channels and synaptic plasticity in the hippocampus. *Neurochem. Int.* 63, 702–711.
- Schweitzer, B., Singh, J., Fejtova, A., Groc, L., Heine, M., and Frischknecht, R. (2017). Hyaluronic acid based extracellular matrix regulates surface expression of GluN2B containing NMDA receptors. *Sci. Rep.* 7, 10991.
- Smith, A.J., and Verkman, A.S. (2015). Superresolution imaging of aquaporin-4 cluster size in antibody-stained paraffin brain sections. *Biophys. J.* 109, 2511–2522.
- Smith, A.J., Jin, B.-J., Ratelade, J., and Verkman, A.S. (2014). Aggregation state determines the localization and function of M1- and M23-aquaporin-4 in astrocytes. *J. Cell Biol.* 204, 559–573.
- Szu, J.I., and Binder, D.K. (2016). The role of astrocytic aquaporin-4 in synaptic plasticity and learning and memory. *Front. Integr. Neurosci.* 10, 8.
- Tardin, C., Cognet, L., Bats, C., Lounis, B., and Choquet, D. (2003). Direct imaging of lateral movements of AMPA receptors inside synapses. *EMBO J.* 22, 4656–4665.
- Theodosios, D.T., and Poulain, D.A. (1993). Activity-dependent neuronal-glia and synaptic plasticity in the adult mammalian hypothalamus. *Neuroscience* 57, 501–535.
- Theodosios, D.T., Poulain, D.A., and Oliet, S.H.R. (2008). Activity-dependent structural and functional plasticity of astrocyte-neuron interactions. *Physiol. Rev.* 88, 983–1008.
- Toulmé, E., Soto, F., Garret, M., and Boué-Grabot, E. (2006). Functional properties of internalization-deficient P2X4 receptors reveal a novel mechanism of ligand-gated channel facilitation by ivermectin. *Mol. Pharmacol.* 69, 576–587.
- Varela, J.A., Dupuis, J.P., Etchepare, L., Espana, A., Cognet, L., and Groc, L. (2016a). Targeting neurotransmitter receptors with nanoparticles in vivo allows single-molecule tracking in acute brain slices. *Nat. Commun.* 7, 10947.
- Varela, J.A., Ferreira, J.S., Dupuis, J.P., Durand, P., Bouchet, D., and Groc, L. (2016b). Single nanoparticle tracking of N-methyl-D-aspartate receptors in cultured and intact brain tissue. *Neurophotonics* 3, 041808.
- Ventura, R., and Harris, K.M. (1999). Three-dimensional relationships between hippocampal synapses and astrocytes. *J. Neurosci.* 19, 6897–6906.
- Volterra, A., and Meldolesi, J. (2005). Astrocytes, from brain glue to communication elements: the revolution continues. *Nat. Rev. Neurosci.* 6, 626–640.
- Wu, X., Zhang, J.T., Li, D., Zhou, J., Yang, J., Zheng, H.L., Chen, J.G., and Wang, F. (2017). Aquaporin-4 deficiency facilitates fear memory extinction in the hippocampus through excessive activation of extrasynaptic GluN2B-containing NMDA receptors. *Neuropharmacology* 112 (Pt A), 124–134.
- Yang, J., Li, M.-X., Luo, Y., Chen, T., Liu, J., Fang, P., Jiang, B., Hu, Z.-L., Jin, Y., Chen, J.-G., and Wang, F. (2013). Chronic ceftriaxone treatment rescues hippocampal memory deficit in AQP4 knockout mice via activation of GLT-1. *Neuropharmacology* 75, 213–222.

STAR★METHODS

KEY RESOURCES TABLE

REAGENT or RESOURCE	SOURCE	IDENTIFIER
Antibodies		
Rabbit anti-GFAP	Dako	Cat.# Z0334
Chicken anti-MAP2	EnCor Biotechnology Inc.	Cat.# CPCA-MAP2
Goat anti-Iba1	Abcam	Cat.# AB5076
Mouse anti-myc	Origene Technologies	Cat.# 9E10
Donkey anti-mouse Alexa A488	Jackson ImmunoResearch	Cat.# 715-545-150
Donkey anti-rabbit Rhodamine TRITC	Jackson ImmunoResearch	Cat.# 711-025-152
Donkey anti-chicken A647	Jackson ImmunoResearch	Cat.# 703-606-155
Rabbit anti-Homer 1/2/3	Synaptic System	Cat.# 160004
Goat anti-rabbit Cy3	Jackson ImmunoResearch	Cat.# 111-165-144
Rabbit anti-AQP4	Merck	Cat.# AB3594
Goat anti-mouse QD 655	Invitrogen	Cat.#Q11021MP
Goat anti-mouse Cy3	Jackson ImmunoResearch	Cat.# 115-166-003
Goat anti-human Alexa A568	Invitrogen	Cat.# A21090
Donkey anti-mouse AlexaFluor 647	Thermo Scientific	Cat.#A31571
Biological samples		
Human anti-AQP4, 0.4 mg ml ⁻¹	Hopital de Lyon	N/A
Human IgG, 0.4 mg ml ⁻¹	Etablissement Français du sang	N/A
Chemicals, Peptides, and Recombinant Proteins		
FM4-64 dye	Molecular Probes	Cat.#T13320
TTX	Tocris	Cat.#1078
glutamate	Sigma-Aldrich	Cat.#56-86-0
bicuculline	Alomone labs	Cat.#B135
nifedipine	Tocris	Cat.#1075
DL-APV	Tocris	Cat.#0105
Experimental Models: Cell Lines		
Rats Sprague-Dawley	Janvier Labs	N/A
Recombinant DNA		
pEnhanced Green Fluorescent Protein (EGFP)	This paper	N/A
pAQP4	Origene	Cat.# SC108945
pAQP4-M1 ^{myc}	This paper	N/A
pAQP4-M23 ^{myc}	This paper	N/A
pGCaMP3	This paper	N/A
Software and Algorithms		
ImageJ	https://imagej.nih.gov/ij/	N/A
MetaMorph	Molecular Devices	N/A
MATLAB	Patel et al., 2015	N/A

LEAD CONTACT AND MATERIALS AVAILABILITY

Further information and requests for resources and reagents should be directed to and will be fulfilled by the Lead Contact, Laurent Groc (laurent.groc@u-bordeaux.fr).

EXPERIMENTAL MODEL AND SUBJECT DETAILS

Cell culture

Mixed hippocampal culture of glia and neurons were prepared from E18 Sprague-Dawley rats, as previously described (Bard et al., 2010; Groc et al., 2004). Dissociated cells were plated at a density of 30×10^4 cells per dish on poly-L-lysine (Sigma-Aldrich) pre-coated diameter glass coverslips. Cultures were maintained in neurobasal medium (GIBCO) with 3% horse serum (vol/vol, Invitrogen) for several days before changing to serum-free neurobasal medium supplemented with B-27 and L-glutamine. Cultures were kept in a humidified incubator at 37°C in 5% CO₂.

Human sera and IgG purification

Sera were obtained from three patients with NMO spectrum disorder, as previously described (Marignier et al., 2016). In addition, we used sera from three healthy blood donors from *Etablissement Français du Sang* (Marignier et al., 2016). According to the French law on bioethics (July 29, 1994; August 6, 2004; and July 7, 2011, Public Health Code), the patients' written informed consent was collected. Moreover, data confidentiality was ensured in accordance with the recommendations of the French commission for data protection (Commission Nationale Informatique et Liberté, CNIL decision DR-2014-558). Sex and age of patients were unknown, as experimentations were performed from blinded sera provided by the Lyon biobank, only characterized by their AQP4-Ab positive serostatus. Briefly, IgG were purified and concentrated to obtain an IgG concentration of 2 mg.ml⁻¹. For cell experiments, IgG were incubated for 30 min.

Organotypic slices

Hippocampal organotypic slices were prepared as previously described (Varela et al., 2016b). Briefly, 350 μm-thick hippocampal slices were obtained from postnatal day 5-7 Sprague-Dawley rats using a McIlwain tissue chopper and were placed in dissection medium containing (in mM): 175 sucrose, 358 D-glucose, 50 NaCl, 0.5 CaCl₂, 2.5 KCl, 0.66 KH₂PO₄, 2 MgCl₂, 0.28 MgSO₄-7H₂O, 0.85 Na₂HPO₄-12H₂O, 2.7 NaHCO₃, 0.5 HEPES pH 7.3 (Sigma). After 25 min incubation, slices were transferred on white FHL membranes (0.45 μm) set on Millicell cell culture inserts (Millipore, 0.4 mm; Ø 30 mm) and cultured for up to 10-14 days on multiwell plates at 35°C/5%CO₂ in a culture medium containing: 200ml basal medium eagle (#41010-026), 100ml Hank's balanced salt solution 1M (#15630056), complemented with 0.45% glucose, 1 mM L-Glutamine, 25% heat inactivated horse serum (# 10368902) (GIBCO). The medium was changed every 2 to 3 days.

METHOD DETAILS

Cell culture transfection

Cells were transfected at 10-12 days *in vitro* (d.i.v.) using Effectene transfection kit (QIAGEN) with plasmids coding for Enhanced Green Fluorescent Protein (EGFP) and AQP4-M1^{myc} or AQP4-M23^{myc} corresponding to AQP4 (Origene-SC108945) with a ten-residue Myc epitope (EQKLISEEDL) in their second extracellular loop (Crane et al., 2008) and maintained between 24-48 hours before experiments. Astrocytes constitute the vast majority of transfected cells and only GFP and AQP4^{myc} co-expressing astrocytes were taken into consideration for analyses. To label synapses, neurons were transfected at d.i.v. 5 with either Homer-dsRed or GCaMP3 plasmids using calcium-phosphate coprecipitation method (Jiang and Chen, 2006). For primary glia cultures (neuron free), cells were diluted to a density of 2×10^5 cells/ml in Dulbecco's modified Eagle Medium (DMEM, Invitrogen) supplemented with 1% glutamax (vol/vol, GIBCO), 1% sodium pyruvate (vol/vol, Sigma-Aldrich) and kept for 20 d.i.v.; neurons were then removed by a mechanical shake of plate.

Immunohistochemistry

In order to immunostain mixed cultures, cells were first fixed with 4% paraformaldehyde/4% sucrose in PBS for 15 min, permeabilized using 0.1% Triton X-100 (vol/vol) and incubated with different primary antibodies overnight: astrocytes were stained with GFAP antibody (1:1000, Dako), neurons with MAP2 antibody (1:500, EnCor Biotechnology Inc), microglia with Iba1 (1:500, Abcam). The day after, cells were incubated with specific secondary antibodies. For endogenous AQP4 staining (Figure S1A), cells were first transfected respectively with no plasmid, eGFP, AQP4-M1^{myc} or AQP4-M23^{myc} and in the latest two samples, incubated for 30 min with antibody to myc (to tag transfected cells). Cells were then fixed, permeabilized and labeled with AQP4 antibody that recognized the intracellular epitope (10 μg/ml, 1 h; Merck-AB3594) and thus mark all AQP4 (both endogenous and exogenous).

For live immunolabeling of AQP4^{myc}, surface AQP4-M1^{myc} or AQP4-M23^{myc} were stained using a monoclonal antibody to Myc (10 μg/ml; clone 9E10, Origene Technologies) for 30 min on lived mixed cultures at 37°C and 5% of CO₂. For live surface labeling of endogenous AQP4, cells were incubated with NMO immunoglobulins (0.4 mg.ml⁻¹, 30 min). Cells were then fixed with 4% paraformaldehyde/4% sucrose in PBS for 15 min, washed and then incubated with appropriate secondary antibodies. Surface AQP4^{myc} staining was compared before and after fixation with 4% paraformaldehyde/4% sucrose in PBS, 15 min. To quantify the cluster area, an Alexa 488 conjugated goat anti mouse (1 h; Jackson ImmunoResearch) was used as secondary antibody. To label Homer, neurons were permeabilized using 0.1% Triton X-100 (vol/vol) and incubated with a primary rabbit polyclonal antibody to Homer 1/2/3 (1:500, 1 h; Synaptic System) and then incubated with a secondary goat antibody to rabbit conjugated with Cyanine 3 (1 h; Jackson

ImmunoResearch). Coverslips were mounted on slides with Vectashield (Vector Laboratories). Immunofluorescence signals were observed with a confocal microscope (Leica DM5500 TCS SPE) equipped with 63X oil objective and 4 diodes laser (405, 488, 561, 635 nm). Images were acquired along the z-axis at 0.5 μm intervals and maximum projection of z stacks was generated. Quantitative analysis was performed with ImageJ (1.50b, NIH). For co-localization study, only AQP4 signals within a pre-defined synaptic area were included. For cluster area, images were analyzed using the Image-based cluster analysis.

Organotypic slices electroporation

Electroporation of cDNA encoding for AQP4-M1^{myc} or AQP4-M23^{myc} and EGFP was performed at d.i.v. 4 using the *Primary Cell Optimization 4D-NucleofectorTM Y Kit* (from Lonza, #V4YP-1A24). Briefly, organotypic slices are cultured within 6-well culture plates on cell culture inserts. For the electroporation step, a 24-well dipping electrode array is inserted into a 24-well plates provided with the kit, after transferring the slices to the wells and adding the specific NucleofectorTM Solution mixed with the cDNA substrate (from 1 to 10 $\mu\text{g}/\mu\text{l}$). For immunohistochemistry, hippocampal slices were first fixed with 4% paraformaldehyde/4% sucrose in PBS for 2 hours, permeabilized using 0.3% Triton X-100 (vol/vol) + 1% BSA for 2 hours and then incubated with NMO immunoglobulines (0.4 $\text{mg}\cdot\text{ml}^{-1}$, overnight). Goat anti-human Alexa 568 antibody (1:1000, 2 hours, Thermo Scientific) was used as secondary antibody. Slices were mounted on slides with Vectashield (Vector Laboratories) and imaged at the same way as described for cultures.

Quantum dots labeling and imaging

In order to track surface AQP4 using single nanoparticle imaging, samples were incubated for 10 min (for primary culture) or 20 min (for organotypic slices) with myc antibody (10 $\mu\text{g}\cdot\text{ml}^{-1}$, 10 min; clone 9E10, Origene Technologies) at 37°C, as previously described (Groc et al., 2007; Varela et al., 2016b). Cells were then washed and incubated respectively for 10-20 min (37°C) with quantum dot (QD) 655 goat F(ab') antibody (1 $\mu\text{g}\cdot\text{ml}^{-1}$; Invitrogen). Non-specific binding was blocked by addition of 1% BSA (vol/vol, Vector Laboratories) to the quantum dot (QD) containing solution. Cells were washed and mounted in a Ludin chamber containing artificial cerebrospinal fluid (aCSF) solution (115 mM NaCl, 1.5 mM KCl, 1.6 mM CaCl_2 , 1.6 mM MgCl_2 , 8.5 mM HEPES and 8.5 mM D-glucose; osmolarity was 250-260 $\text{mosm}\cdot\text{kg}^{-1}$; pH 7.4). The lateral diffusion of AQP4-M1^{myc} and AQP4-M23^{myc} was recorded with a Nikon microscope (NIKON Eclipse TE2000-U) with a stage heated to 37°C using an air blower (World Precision Instruments) and an objective heater (Biopetechs). QD were detected using a mercury lamp and appropriate excitation/emission filters. Images were recorded with an integration time of 50 ms for 500 consecutive frames (25 s) and signals were detected using an EM-CCD camera, and image analysis performed using MetaMorph software (Molecular Devices). QD were followed on randomly selected GFP-expressing astrocytes and tagged with AQP4-M1^{myc} or AQP4-M23^{myc}. The instantaneous diffusion coefficient “D” was calculated for each trajectory, from linear fits of the first four points of the mean square displacement versus time function using $MSD(t) = \langle r^2 \rangle (t) = 4Dt$. The two-dimensional trajectories of single molecules in the plane of focus were reconstructed by correlation analysis between consecutive images using a Vogel algorithm. Synaptic dwell-time was calculated and defined as the mean time spent in the synaptic area (defined as the Homer cluster + 500 nm annulus around it). For different experimental conditions, antibody or drugs were added to the bath: x-link (same antibody against the myc tag as the one used for surface tracking but at higher concentration: 200 $\mu\text{g}\cdot\text{ml}^{-1}$, 30 min, clone 9E10, Origene Technologies), NMO-IgG or healthy-IgG (0.4 $\text{mg}\cdot\text{ml}^{-1}$, 30 min), TTX (1 μM , 20 min; Tocris), L-glutamate (100 μM , 20 min, Sigma-Aldrich). For the acid wash experiment (Tardin et al., 2003) (Figure S1C), a low pH (pH 2) of aCSF at 4°C was used. Cells were imaged and left for 10, 15, 20 and 30 min intervals before 1 min of incubation with cold aCSF (pH 2) to break antibody-proteins bonds and so the only transporters with QDs still attached are the ones that have been internalised. Another QD imaging series was acquired after removing and replacing with aCSF pH 7.4 at 37°C.

dSTORM and Image-based cluster analysis

For dSTORM experiments, at d*iv* 12-14 live transfected cells were first incubated with 1% BSA (Sigma-A3059) added directly in the culture dish for 5 min at 37°C and specifically stained for surface myc labeling (10 $\mu\text{g}/\text{ml}$; anti-myc, clone 9E10, Origene Technologies) for 30 min at 37°C. Fixation using 4% paraformaldehyde/4% sucrose in PBS (15 min, room temperature) was followed by a 40 min blocking step with a solution containing 1.5% bovine serum albumin/0.1% fish skin gelatine (Sigma-G7765) 0.1% Triton X-100 for 40 min. Cells were then incubated with anti-mouse AlexaFluor647 (Thermo Scientific-A31571, 1 $\mu\text{g}/\text{ml}$) during 30 min and fixed for a second time in order to avoid dissociation of the labeling before image acquisition. The labeled astrocytes were imaged within 24 hours using a commercial Leica GSDIM super-resolution microscope (Leica Microsystems, Wetzlar, Germany). The microscope was fitted with an HC PL APO 160x 1.43 NA oil immersion TIRF objective (Leica) enabling detection of single fluorophores. For dSTORM imaging, the samples were mounted in a closed Ludin chamber containing an extracellular switching buffer supplemented with oxygen scavengers and reducing agents. Photoswitchable AlexaFluor647 was excited in TIRF mode using first a high 642 nm laser power (50% of full power) to achieve single molecule blinking, followed by a lower power (15% of full power) during the acquisition. The intensity of the 405 nm laser (30 mW) was continuously adjusted in order to keep an optimal number of stochastically activated molecules. Fluorescence emission of the AlexaFluor647 was detected by an EMCCD iXon camera (ANDOR, Belfast, UK) with an exposure time of 10.85 ms in a total of 100.000 consecutive frames. Particle detection threshold was set to 20 in the Leica LAS software and multicolor fluorescent microbeads (T7279 TetraSpeck, Life Technologies) were used for lateral drift correction. dSTORM images were reconstructed using a fitting algorithm by the Leica LAS software using a 2-dimensional Gaussian fitting

algorithm. These images were then analyzed using ImageJ software (ImageJ 1.50b, NIH). Briefly, images were thresholded and the analyze particles function was used to determine the number and area of AQP4-M1 and AQP4-M23 clusters, respectively.

Time-lapse imaging and analysis

For time-lapse experiments, cells were transfected with GFP and AQP4-M1^{myc} or AQP4-M23^{myc} before live immunostaining for AQP4^{myc} using a monoclonal antibody to myc (10 $\mu\text{g/ml}$, 15 min; clone 9E10, Origene Technologies) followed by a secondary goat antibody to mouse conjugated with Cy3 (15 min; Jackson ImmunoResearch). For time-lapse experiments with labeled synapses, presynaptic terminals were labeled with 10 μM of FM4-64 dye (Molecular Probes-T13320) in a solution containing 60 mM of KCl at the end of each acquisition. Time-lapse imaging was performed on a Spinning-disk LIFA microscope (Leica DMI6000B) with a 40X dry objective, with four diodes laser (408, 491, 561, 638 nm) and a stage heated to 37°C. Z-stacks of GFP labeling were acquired every minute during 30 min using MetaMorph software (Molecular Devices). Quantitative analysis was performed with ImageJ software. Briefly, maximum projection of z stacks was generated followed by x,y-axis movement correction using stackreg plugin. Images were then thresholded, filtered with 3x3 mean filter and binarized (Bernardinelli et al., 2014). The area of processes for each time point was finally calculated. Changes in area (astrocytic movement) over time were measured from the standard deviation of 30 images over time (Figures S2A and S2B). For experiments with labeled synapses, only GFP-expressing astrocytes within a pre-defined synaptic area were included. For different experimental conditions, antibody or drugs were added to the bath: x-link (200 $\mu\text{g.ml}^{-1}$, clone 9E10, Origene Technologies, 30 min), NMO-IgG or healthy-IgG (0.4 mg.ml^{-1} , 30 min), TTX (1 μM , 20 min; Tocris), L-glutamate (100 μM , 20 min, Sigma-Aldrich).

Osmotic swelling assay

Oocytes were removed from *Xenopus laevis* as previously described (Jo et al., 2011; Toulmé et al., 2006). After nuclear injection of cDNAs coding for AQP4-M1^{myc} or AQP4-M23^{myc} (300 pg each), oocytes were incubated in Barth's solution containing 1.8 mM CaCl_2 , pyruvic acid (0.5 mg/ml) and gentamycin (50 $\mu\text{g/ml}$, Sigma-Aldrich) at 19°C for 2-3 days before experiments. Oocytes were then exposed to myc antibody (10 $\mu\text{g.ml}^{-1}$ or 200 $\mu\text{g.ml}^{-1}$ for x-link experiments, 30 min, clone 9E10, Origene Technologies) or NMO-IgG or healthy-IgG (0.4 mg.ml^{-1} , 30 min) and then immersed to distilled water (Madeira et al., 2016). Lysis time was observed with a MacroScope Leica Z 16 APO. To confirm that the cell swelling was due to the presence of AQP4, we exposed the oocytes with two AQP4 inhibitors: bumetanide (75 μM ; Sigma-Aldrich-B3023) intracellularly injected and TGN-020 (500 μM ; Sigma-Aldrich-SML0136) in the extracellular solution for 30 min before immersion into water. Death rate and fold in lysis time were calculated by comparing the average of live oocytes from three independent experiments.

Calcium imaging and analysis

For calcium imaging experiments, neurons were transfected with GCaMP3 and astrocytes with GFP/AQP4-M1^{myc} or GFP/AQP4-M23^{myc} plasmids before live immunostaining for AQP4^{myc} using a monoclonal antibody to myc (10 $\mu\text{g/ml}$, 15 min; clone 9E10, Origene Technologies) followed by a secondary goat antibody to mouse conjugated with Cy3 (15 min; Jackson ImmunoResearch). Calcium imaging was performed after 15 min of incubation in aCSF Mg^{2+} free solution (110 mM NaCl, 5 mM KCl, 2 mM CaCl_2 , 8.5 mM HEPES and 8.5 mM D-glucose; osmolarity was 250-260 mosml kg^{-1} ; pH 7.4) with Ca^{2+} current blockers bicuculline (5 μM ; Alomone labs-B135) and nifedipine (5 μM ; Tocris). Changes in GCaMP3 signal were acquired with Spinning-disk LIFA microscope (Leica DMI6000B) with a 63X oil objective, an EMCCD camera and a stage heated to 37°C. Images were acquired at 20 Hz with 50 ms of exposure time. DL-APV (50 μM ; Tocris-0105) was added at the end of experiments for 5 min before images recorded. Calcium signal was detected from randomly selected GCaMP3 neurons facing astrocytes tagged with AQP4-M1^{myc} or AQP4-M23^{myc} and recorded with MetaMorph software. Data analysis were carried out as described in Patel et al. Briefly, ROIs of spines were first delineated and the fluorescence versus time trace was calculated with MATLAB script (Patel et al., 2015). The fluorescence ratio ($\Delta F/F$) was quantified and a threshold at 0.2 was used to determine peak calcium fluorescence.

QUANTIFICATION AND STATISTICAL ANALYSIS

All quantitated analysis were performed with the researcher blind to the condition.

All data were acquired from at least three independent batches of cells. Detailed for experiment parameters are provided in the Supplemental Data Analysis Table S1. Data are presented as mean \pm s.e.m., median \pm IQR or standard deviation. All statistical tests were carried out using GraphPad Prism 6.0. Significance was assessed by performing the Mann-Whitney U, the Pearson correlation test, One-way ANOVA and Student's t test.